

**SYNTHESIS, CHARACTERIZATION, NUCLEOLYTIC,
ANTIBACTERIAL AND ANTIPROLIFERATIVE
PROPERTIES OF VANADIUM, COPPER AND
MANGANESE COMPLEXES**

LIM ENG KHOON

Thesis submitted in fulfillment of the requirements

for the degree of

Doctor of Philosophy

July 2011

ACKNOWLEDGEMENTS

I would like to express profound gratitude to my supervisor, Professor Dr. Teoh Siang Guan, for his invaluable support, encouragement, enthusiasm, supervision and useful suggestions throughout this research work. His moral support and continuous guidance enabled me to complete my work successfully. I am also highly thankful to Associate Professor Dr. Ng Chew Hee, Faculty of Engineering and Science, Universiti Tunku Abdul Rahman, Professor Dr. Mohd Nazalan Mohd Najimudin, School of Biological Sciences, Universiti Sains Malaysia and Professor Dr. Tengku Sifzizul Tengku Muhammad, School of Biological Sciences, Universiti Sains Malaysia, for their valuable suggestions throughout this study.

I would also like to express my deep appreciation to Professor Dr. Fun Hoong Kun and Mr. Mohd Mustaqim Rosli, X-ray Crystallography Unit, School of Physics, Universiti Sains Malaysia, for their professional guidance, excellent help and valuable advice for running and analysis all my X-ray Crystallography samples.

Special thanks go to Miss Beh Hooi Kheng and Miss Seow Lay Jing, School of Pharmaceutical Sciences, Universiti Sains Malaysia; Mr. Cheah Yew Hoong, Bioassay Unit, Herbal Medicine Research Center, Institute Medical Centre; Miss Chew Guat Siew, Mr. Yam Hok Chai, Mr. Yuen Chee Wah and Mr. Emmanuel Jairaj Moses, School of Biological Sciences, Universiti Sains Malaysia, for their guidance and help in the biological tests.

I want to give my thanks to the staff of the School of Chemical Science, Universiti Sains Malaysia, especially to Mr. Aw Yeong Choek Hoe, Mr. Ong Chin Hwie, Mr. Ong Ching Hin, Mr. Razli Effendy bin Khalidee, Mr. Marimuthu Ayeroo, Pn. Hjh. Zali Zaiton Hj. Hussin, Pn. Yeoh Chooi Ling, Mr. Ahmad Azrulhisham Abdul Rahim, Mr. Mohd Kassim Abd Razak, Mr. Yee Chin Leng and Mr. Clement D' Silva, for their constant help and support throughout my study.

I am also sincerely grateful to USM Fellowship award from Institute of Postgraduate Studies (IPS), Universiti Sains Malaysia, for the financial support and RU Grant and Science Fund from Universiti Sains Malaysia, and FRGS Grant from Ministry of Higher Education (MOHE), Malaysia, for funding this research.

I also like to express my warmest gratitude to my friends, especially to Sharon Fatinathan, Yasodha Sivasothy, Ong Chin Hin, Oo Chuan Wei, Vijay, Yoga, Wendy, Mandy, Cynn Dee, William Yip, Karen Onn and many more, for their moral support and kindness.

Finally, I would like to thank my family members, especially my wife, Belle, for supporting and encouraging me to pursue this degree. Without my family encouragement, I would not have finished the degree.

To all of you, I say *Ribuan Terima Kasih*

TABLE OF CONTENTS

	Page
Title page	i
Acknowledgements	ii
Table of Contents	iv
List of Figures	xi
List of Tables	xxxv
List of Abbreviations and Symbols	xlii
Abstract in Bahasa Malaysia	xlv
Abstract in English	xlvii
CHAPTER 1 INTRODUCTION	1
1.1 Biological roles and medicinal applications of metal complexes and metal ions	1
1.2 Antibacterial and antiproliferative activities of transition metal complexes	4
1.3 Background of nucleolytic activity of metal complexes	7
1.3.1 Oxidative DNA cleavage by metal complexes in the presence of 3-mercaptopropionic acid (MPA)	12
1.3.2 Oxidative DNA cleavage by metal complexes in the presence of ascorbic acid	14
1.3.3 Oxidative DNA cleavage by metal complexes in the presence of H ₂ O ₂	16
1.3.4 Photolytic DNA cleavage by metal complexes	18
1.3.5 Hydrolytic DNA cleavage by metal complexes	21
1.3.6 Oxidative DNA cleavage by copper(II) amino acid complexes in the presence of H ₂ O ₂	23
1.4 DNA-metal complexes interaction	25
1.5 Research Objective	27

TABLE OF CONTENTS

	Page
CHAPTER 2 EXPERIMENTAL	29
2.1 Reagents and materials	29
2.2 Instruments	29
2.3 X-ray crystallography	31
2.4 DNA cleavage experiments	31
2.5 DNA binding absorption studies	32
2.6 Antibacterial screening (inhibition zone)	33
2.7 Antibacterial screening (MIC)	33
2.8 Cell line and cell culture	34
2.9 In vitro cytotoxic assay (Sulforhodamine B (SRB))	34
2.10 MTT (3-[4,5-dimethylthiazol-2-yl]-2,5-diphenyl tetrazolium bromide) assay	36
2.11 Synthesis	37
2.11.1 Synthesis of complex VO₂PP	38
2.11.2 Synthesis of complex VO₂GLY	39
2.11.3 Synthesis of complex VOPYDC	39
2.11.4 Synthesis of complex VOMAL	40
2.11.5 Synthesis of complex VO₂HPYDC	40
2.11.6 Synthesis of complexes Cu-4-Cl-2-NO₂BZO , Cu-2-Cl-6-FBZO , Cu-2-CIBZO and Cu-2-BrBZO	41
2.11.7 Synthesis of complexes Cu-2-Cl-4-NO₂BZO , CuP-5-Cl-2-NO₂BZO and Cu-2-F-6-FBZO	42

TABLE OF CONTENTS

	Page
2.11.8 Synthesis of complexes MnP-4-Cl-2-NO₂BZO, MnP-3-NO₂-5-NO₂BZO, Mn-4-NO₂BZO, MnP-4-NH₂BZO, MnP-4-FBZO, MnP-4-CIBZO and MnPGLY	44
2.11.9 Synthesis of complex MnP_{yr}	46
2.11.10 Synthesis of complexes VOPhen, VODMPhen, VODPPhen and VODMPPhen	46
CHAPTER 3 Characterization, Nucleolytic, Antibacterial and Antiproliferative Properties of Vanadium Carboxylato Complexes	48
Results and Discussion	
3.1 X-ray crystallography analysis of complex VO₂PP	48
3.2 X-ray crystallography analysis of complex VO₂GLY	53
3.3 X-ray crystallography analysis of complex VOPYDC	58
3.4 FT-IR analysis of complexes VO₂PP, VO₂GLY and VO₂HPYDC	63
3.5 FT-IR analysis of complexes VOPYDC and VOMAL	69
3.6 UV-Vis analysis of complexes VO₂PP, VO₂GLY, VO₂HPYDC, VOPYDC and VOMAL	74
3.7 ⁵¹ V-NMR analysis of complexes VO₂PP, VO₂GLY, VO₂HPYDC, VOPYDC and VOMAL	83
3.8 Redox property of complexes VO₂PP, VO₂GLY, VOPYDC, VOMAL and VO₂HPYDC	88
3.9 DNA cleavage activity of complexes VO₂PP, VO₂GLY, VOPYDC, VOMAL and VO₂HPYDC	93
3.10 Comparison of DNA cleavage activity of complexes VO₂PP, VO₂GLY, VOPYDC, VOMAL and VO₂HPYDC	100

TABLE OF CONTENTS

	Page
3.11 DNA cleavage mechanism study of complexes VO₂PP, VO₂GLY, VOPYDC, VOMAL and VO₂HPYDC	102
3.12 Antibacterial activity of complexes VO₂PP, VO₂GLY, VOPYDC, VOMAL and VO₂HPYDC	107
3.13 Antiproliferative activity of complexes VO₂PP, VO₂GLY, VOPYDC, VOMAL and VO₂HPYDC	110
CHAPTER 4 Characterization, Nucleolytic, Antibacterial and Antiproliferative Properties of Copper Carboxylate Complexes	113
4.1 X-ray crystallography analysis of complexes Cu-4-Cl-2-NO₂BZO, Cu-2-Cl-4-NO₂BZO, Cu-2-Cl-6-FBZO, Cu-2-F-6-FBZO, Cu-2-CIBZO and Cu-2-BrBZO	113
4.2 X-ray crystallography analysis of complex CuP-5-Cl-2-NO₂BZO	136
4.3 FT-IR analysis of complexes Cu-4-Cl-2-NO₂BZO, Cu-2-Cl-4-NO₂BZO, CuP-5-Cl-2-NO₂BZO, Cu-2-Cl-6-FBZO, Cu-2-F-6-FBZO, Cu-2-CIBZO and Cu-2-BrBZO	142
4.4 UV-Vis analysis of complexes Cu-4-Cl-2-NO₂BZO, Cu-2-Cl-4-NO₂BZO, CuP-5-Cl-2-NO₂BZO, Cu-2-Cl-6-FBZO, Cu-2-F-6-FBZO, Cu-2-CIBZO and Cu-2-BrBZO	153
4.5 Redox property of complexes Cu-4-Cl-2-NO₂BZO, Cu-2-Cl-4-NO₂BZO, CuP-5-Cl-2-NO₂BZO, Cu-2-Cl-6-FBZO, Cu-2-F-6-FBZO, Cu-2-CIBZO and Cu-2-BrBZO	163
4.6 DNA cleavage activity of complexes Cu-4-Cl-2-NO₂BZO, Cu-2-Cl-4-NO₂BZO, CuP-5-Cl-2-NO₂BZO, Cu-2-Cl-6-FBZO, Cu-2-F-6-FBZO, Cu-2-CIBZO and Cu-2-BrBZO	168
4.7 Comparison of DNA cleavage activity of complexes Cu-4-Cl-2-NO₂BZO, Cu-2-Cl-4-NO₂BZO, CuP-5-Cl-2-NO₂BZO, Cu-2-Cl-6-FBZO, Cu-2-F-6-FBZO, Cu-2-CIBZO and Cu-2-BrBZO	176

TABLE OF CONTENTS

	Page
4.8 DNA cleavage mechanism studies of complexes Cu-4-Cl-2-NO₂BZO, Cu-2-Cl-4-NO₂BZO, CuP-5-Cl-2-NO₂BZO, Cu-2-Cl-6-FBZO, Cu-2-F-6-FBZO, Cu-2-CIBZO and Cu-2-BrBZO	178
4.9 Antibacterial activity of complexes Cu-4-Cl-2-NO₂BZO, Cu-2-Cl-4-NO₂BZO, CuP-5-Cl-2-NO₂BZO, Cu-2-Cl-6-FBZO, Cu-2-F-6-FBZO, Cu-2-CIBZO and Cu-2-BrBZO	184
4.10 Antiproliferative activity of complexes Cu-4-Cl-2-NO₂BZO, Cu-2-Cl-4-NO₂BZO, CuP-5-Cl-2-NO₂BZO, Cu-2-Cl-6-FBZO, Cu-2-F-6-FBZO and Cu-2-CIBZO	188
CHAPTER 5 Characterization, Nucleolytic, Antibacterial and Antiproliferative Properties of Manganese Carboxylato Complexes	192
Results and Discussion	
5.1 X-ray crystallography analysis of complexes MnP-4-Cl-2-NO₂BZO, MnP-3-NO₂-5-NO₂BZO and Mn-4-NO₂BZO	192
5.2 X-ray crystallography analysis of complex MnP-4-NH₂BZO	203
5.3 X-ray crystallography analysis of complex MnP-4-FBZO	208
5.4 X-ray crystallography analysis of complex MnPGLY	213
5.5 FT-IR analysis of complexes MnP-4-Cl-2-NO₂BZO, MnP-3-NO₂-5-NO₂BZO, Mn-4-NO₂BZO, MnP-4-NH₂BZO, MnP-4-FBZO, MnP-4-CIBZO, MnPGLY and MnPyr	218
5.6 UV-Vis analysis of complexes MnP-4-Cl-2-NO₂BZO, MnP-3-NO₂-5-NO₂BZO, Mn-4-NO₂BZO, MnP-4-NH₂BZO, MnP-4-FBZO, MnP-4-CIBZO, MnPGLY and MnPyr	231
5.7 Redox property of complexes MnP-4-Cl-2-NO₂BZO, MnP-3-NO₂-5-NO₂BZO, Mn-4-NO₂BZO, MnP-4-NH₂BZO, MnP-4-FBZO, MnP-4-CIBZO, MnPGLY and MnPyr	242

TABLE OF CONTENTS

	Page
5.8 DNA cleavage activity of complexes MnP-4-Cl-2-NO₂BZO, MnP-3-NO₂-5-NO₂BZO, Mn-4-NO₂BZO, MnP-4-NH₂BZO, MnP-4-FBZO, MnP-4-CIBZO, MnPGLY and MnPyr	249
5.9 Comparison of DNA cleavage activity of complexes MnP-4-Cl-2-NO₂BZO, MnP-3-NO₂-5-NO₂BZO, Mn-4-NO₂BZO, MnP-4-NH₂BZO, MnP-4-FBZO, MnP-4-CIBZO, MnPGLY and MnPyr	258
5.10 DNA cleavage mechanism studies of complexes MnP-4-Cl-2-NO₂BZO, MnP-3-NO₂-5-NO₂BZO, Mn-4-NO₂BZO, MnP-4-NH₂BZO, MnP-4-FBZO, MnP-4-CIBZO, MnPGLY and MnPyr	260
5.11 Antibacterial activity of complexes MnP-4-Cl-2-NO₂BZO, MnP-3-NO₂-5-NO₂BZO, Mn-4-NO₂BZO, MnP-4-NH₂BZO, MnP-4-FBZO, MnP-4-CIBZO, MnPGLY and MnPyr	265
5.12 Antiproliferative activity of complexes MnP-4-Cl-2-NO₂BZO, MnP-3-NO₂-5-NO₂BZO, Mn-4-NO₂BZO, MnP-4-NH₂BZO and MnPyr	268
CHAPTER 6 Characterization, Nucleolytic, Antibacterial and Antiproliferative Properties of Vanadium(IV) Phenanthroline Derivative Complexes	270
Results and Discussion	
6.1 Characterization of complexes VOPhen, VODMPhen, VODPPhen and VODMPPhen	270
6.2 DNA binding studies	278
6.2.1 Electronic absorption spectra study of complexes VOPhen, VODMPhen, VODPPhen and VODMPPhen	278
6.2.2 Viscosity study of complexes VOPhen, VODMPhen, VODPPhen and VODMPPhen	288
6.2.3 Circular dichroism (CD) study of complexes VOPhen, VODMPhen, VODPPhen and VODMPPhen	290

TABLE OF CONTENTS

	Page
6.3 DNA cleavage activity of complexes VOPhen, VODMPhen, VODPPhen and VODMPPhen	291
6.4 Comparison of DNA cleavage activity of complexes VOPhen, VODMPhen, VODPPhen and VODMPPhen	296
6.5 Antibacterial and antiproliferative activities of complexes VOPhen, VODMPhen, VODPPhen and VODMPPhen	300
6.6 The insight of antibacterial and antiproliferative activities of vanadium carboxylato complexes and vanadium phenanthroline derivative complexes	304
CHAPTER 7 CONCLUSION	306
REFERENCES	307
APPENDICES	318
PUBLICATIONS	320

LIST OF FIGURES

		Page
Figure 1.1	Schematic structures of cisplatin, carboplatin and oxaliplatin	2
Figure 1.2	The structure of part of a DNA double helix	8
Figure 1.3	The chemical structure of DNA. Hydrogen bonds are shown as dotted lines.	9
Figure 1.4	Supercoiled, nicked and linear DNA	11
Figure 1.5	Supercoiled, nicked and linear DNA bands in gel electrophoresis diagram	12
Figure 1.6	The schematic structures; a) $[\text{Cu}^{\text{II}}(\text{ternary-L-glutamine})(1,10\text{-phenanthroline})(\text{H}_2\text{O})](\text{ClO}_4)$ b) $[\text{Cu}^{\text{II}}(\text{ternary-S-methyl-L-cysteine})(1,10\text{-phenanthroline})(\text{H}_2\text{O})](\text{ClO}_4)$	13
Figure 1.7	The proposed DNA cleavage mechanism of metal complex in the presence of 3-mercaptopropionic acid (MPA)	13
Figure 1.8	The schematic structures; a) $[\text{Ru}^{\text{II}}(\text{imidazo}[4,5\text{-f}][1,10]\text{phenanthroline})(\text{NH}_3)_4](\text{PF}_6)_2$ b) $[\text{Cu}^{\text{II}}(\text{L-threonine})(1,10\text{-phenanthroline})(\text{H}_2\text{O})](\text{ClO}_4)$	15
Figure 1.9	The proposed DNA cleavage mechanism of metal complex in the presence of ascorbic acid	15
Figure 1.10	The schematic structures; a) $[\text{Co}^{\text{II}}(\text{imidazole-terpyridine})_2](\text{ClO}_4)_2$ b) $[\text{Cu}^{\text{II}}(\text{imidazole terpyridine})_2](\text{ClO}_4)_2$	17
Figure 1.11	The proposed DNA cleavage mechanism of metal complex in the presence of H_2O_2	17
Figure 1.12	The schematic structures; a) $[\text{Cu}^{\text{II}}(\text{ternary-S-methyl-L-cysteine})(\text{dipyridoquinoxaline})(\text{H}_2\text{O})](\text{ClO}_4)$ b) $[\text{Co}^{\text{III}}(\text{ethylenediamine})_2(\text{imidazo}[4,5\text{-f}][1,10]\text{-phenanthroline})]\text{Br}_3$	19

LIST OF FIGURES

		Page
Figure 1.12	The schematic structures; c) $[\text{Ru}^{\text{II}}(2,2'\text{-bipyridine})_2(5\text{-methoxy-isatino-[1,2-b]-1,4,8,9-tetraazatriphenylene)}](\text{ClO}_4)_2$ d) $[\text{Ni}^{\text{II}}(\text{naphtho[2,3-}a\text{]dipyrido[3,2-}h\text{:2',3'-}f\text{]phenazine-5,18-dione})(1,10\text{-phenanthroline})](\text{PF}_6)$	20
Figure 1.13	The proposed DNA cleavage mechanism of metal complex upon irradiation	21
Figure 1.14	The schematic structures; a) $[\text{Co}^{\text{III}}(\text{bis}[2\text{-(2-pyridylethyl)]-(2-pyridylmethyl)amine})(\text{OH})(\text{H}_2\text{O})]^{2+}$ b) $[\text{Mn}^{\text{II}}(\text{quercetin})_2(\text{H}_2\text{O})_2]\text{Cl}_2$	22
Figure 1.15	The proposed hydrolytic DNA cleavage mechanism by the metal complex	23
Figure 1.16	The schematic structures; a) $\text{Cu}^{\text{II}}(\text{N,N}'\text{-dimethylglycinato})_2$ b) $\text{Cu}^{\text{II}}(\text{N,N-di-}(N'\text{-methylacetamido})\text{-L-alaninato})_2$	24
Figure 1.17	Complexes bind with DNA via hydrogen bonding	25
Figure 1.18	Complexes bind with DNA via electrostatic interaction	26
Figure 1.19	Complexes binds with DNA via intercalation	26
Figure 3.1	The molecular structure of complex VO₂PP , showing 50 % probability displacement ellipsoids and the atomic numbering (Refer to the list of Publication at page 325)	50
Figure 3.2	The crystal packing of complex VO₂PP	51
Figure 3.3	The molecular structure of complex VO₂GLY , showing 50 % probability displacement ellipsoids and the atomic numbering	55
Figure 3.4	The crystal packing of complex VO₂GLY	56

LIST OF FIGURES

		Page
Figure 3.5	The molecular structure of complex VOPYDC , showing 50 % probability displacement ellipsoids and the atomic numbering (Refer to the list of Publication at page 325)	60
Figure 3.6	The crystal packing of complex VOPYDC	61
Figure 3.7(A)	FT-IR spectrum of complex VO₂PP	66
Figure 3.7(B)	FT-IR spectrum of 2-picolinic acid	66
Figure 3.8(A)	FT-IR spectrum of complex VO₂GLY	67
Figure 3.8(B)	FT-IR spectrum of diglycolic acid	67
Figure 3.9	Chemical structure of complex VO₂HPYDC [72]	68
Figure 3.10(A)	FT-IR spectrum of complex VO₂HPYDC	68
Figure 3.10(B)	FT-IR spectrum of 4-hydroxypyridine-2,6-dicarboxylic acid	69
Figure 3.11(A)	FT-IR spectrum of complex VOPYDC	72
Figure 3.11(B)	FT-IR spectrum of pyridine-2,6-dicarboxylic acid	72
Figure 3.12	Chemical structure of complex VOMAL [71]	73
Figure 3.13(A)	FT-IR spectrum of complex VOMAL	73
Figure 3.13(B)	FT-IR spectrum of malonic acid	74
Figure 3.14(A)	UV-Vis spectrum of complex VO₂PP ($9.94 \times 10^{-3} \text{ mol L}^{-1}$)	77
Figure 3.14(B)	UV-Vis spectrum of complex VO₂PP ($3.96 \times 10^{-5} \text{ mol L}^{-1}$; $\lambda = 262 \text{ nm}$, $\epsilon = 10\,295 \text{ mol}^{-1}\text{Lcm}^{-1}$; $\lambda = 204 \text{ nm}$, $\epsilon = 20\,485 \text{ mol}^{-1}\text{Lcm}^{-1}$)	77
Figure 3.15(A)	UV-Vis spectrum of complex VO₂GLY (0.014 mol L^{-1})	78
Figure 3.15(B)	UV-Vis spectrum of complex VO₂GLY ($5.47 \times 10^{-5} \text{ mol L}^{-1}$; $\lambda = 259 \text{ nm}$, $\epsilon = 2945 \text{ mol}^{-1}\text{Lcm}^{-1}$; $\lambda = 203 \text{ nm}$, $\epsilon = 7310 \text{ mol}^{-1}\text{Lcm}^{-1}$)	78

LIST OF FIGURES

		Page
Figure 3.16(A)	UV-Vis spectrum of complex VO₂HPYDC (0.012 mol L ⁻¹)	79
Figure 3.16(B)	UV-Vis spectrum of complex VO₂HPYDC (9.18 x 10 ⁻⁶ mol L ⁻¹ ; A = 276 nm, ε = 12 730 mol ⁻¹ Lcm ⁻¹ ; A = 203 nm, ε = 44 762 mol ⁻¹ Lcm ⁻¹)	79
Figure 3.17(A)	UV-Vis spectrum of complex VOPYDC (0.013 mol L ⁻¹ ; A = 836 nm, ε = 26 mol ⁻¹ Lcm ⁻¹ ; A = 616 nm, ε = 16 mol ⁻¹ Lcm ⁻¹)	80
Figure 3.17(B)	UV-Vis spectrum of complex VOPYDC (2.57 x 10 ⁻⁵ mol L ⁻¹ ; A = 268 nm, ε = 5512 mol ⁻¹ Lcm ⁻¹ ; A = 207 nm, ε = 18 648 mol ⁻¹ Lcm ⁻¹)	80
Figure 3.18(A)	UV-Vis spectrum of complex VOMAL (0.011 mol L ⁻¹ ; A = 804 nm, ε = 36 mol ⁻¹ Lcm ⁻¹ ; A = 595 nm, ε = 12 mol ⁻¹ Lcm ⁻¹)	81
Figure 3.18(B)	UV-Vis spectrum of complex VOMAL (4.45 x 10 ⁻⁵ mol L ⁻¹ ; A = 263 nm, ε = 1689 mol ⁻¹ Lcm ⁻¹ ; A = 203 nm, ε = 8025 mol ⁻¹ Lcm ⁻¹)	81
Figure 3.19	UV-Vis spectrum of NaVO ₃ (0.016 mol L ⁻¹)	82
Figure 3.20	UV-Vis spectrum of VOSO ₄ (0.024 mol L ⁻¹ ; A = 777 nm, ε = 11 mol ⁻¹ Lcm ⁻¹ ; A = 614 nm, ε = 5 mol ⁻¹ Lcm ⁻¹)	82
Figure 3.21(A)	⁵¹ V-NMR spectrum of complex VO₂PP (300.0 K)	85
Figure 3.21(B)	⁵¹ V-NMR spectrum of complex VO₂GLY (300.0 K)	85
Figure 3.21(C)	⁵¹ V-NMR spectrum of complex VO₂HPYDC (300.0 K)	86
Figure 3.21(D)	⁵¹ V-NMR spectrum of complex VOPYDC (300.0 K)	86
Figure 3.21(E)	⁵¹ V-NMR spectrum of complex VOMAL (300.0 K)	87
Figure 3.22	⁵¹ V-NMR spectrum of NaVO ₃ (300.0 K)	87
Figure 3.23	⁵¹ V-NMR spectrum of complex VOSO ₄ (300.0 K)	88

LIST OF FIGURES

		Page
Figure 3.24(A)	Cyclic voltammogram of complex VO₂PP ; Epa = anodic oxidation peak, Epc = cathodic reduction peak	90
Figure 3.24(B)	Cyclic voltammogram of complex VO₂GLY ; Epa = anodic oxidation peak, Epc = cathodic reduction peak	91
Figure 3.24(C)	Cyclic voltammogram of complex VOPYDC ; Epa = anodic oxidation peak, Epc = cathodic reduction peak	91
Figure 3.24(D)	Cyclic voltammogram of complex VOMAL ; Epa = anodic oxidation peak, Epc = cathodic reduction peak	92
Figure 3.24(E)	Cyclic voltammogram of complex VO₂HPYDC ; Epa = anodic oxidation peak, Epc = cathodic reduction peak	92
Figure 3.25	Cleavage of supercoiled pBR322 by complex VO ₂ PP at different concentrations in phosphate buffer pH 7.5. L1 Gene Ruler 1 kb DNA ladder, L2, DNA alone; L3, H ₂ O ₂ alone; L4, complex alone (6 mM); Lanes 5-12 DNA with increasing concentration of complex + H ₂ O ₂ : lane 5, 10 μM; lane 6, 50 μM; lane 7, 1 mM; lane 8, 2 mM; lane 9, 3 mM; lane 10, 4 mM; lane 11, 5 mM; lane 12, 6 mM.	94
Figure 3.26	Gene Ruler 1 kb DNA ladder, unit in bp (base pair)	95
Figure 3.27	Cleavage of supercoiled pBR322 by complex VO₂GLY at different concentrations in phosphate buffer pH 7.5. L1 Gene Ruler 1 kb DNA ladder, L2, DNA alone; L3, H ₂ O ₂ alone; L4, complex alone (6 mM); Lanes 5-12 DNA with increasing concentration of complex + H ₂ O ₂ : lane 5, 10 μM; lane 6, 50 μM; lane 7, 1 mM; lane 8, 2 mM; lane 9, 3 mM; lane 10, 4 mM; lane 11, 5 mM; lane 12, 6 mM.	96
Figure 3.28	Cleavage of supercoiled pBR322 by complex VOPYDC at different concentrations in phosphate buffer pH 7.5. L1 Gene Ruler 1 kb DNA ladder, L2 DNA alone, Lanes 3-12 DNA with increasing concentration of complex: lane 3, 50 μM; lane 4, 100 μM; lane 5, 200 μM; lane 6, 300 μM; lane 7, 400 μM; lane 8, 500 μM; lane 9, 600 μM; lane 10, 700 μM; lane 11, 800 μM; lane 12, 900 μM.	97
Figure 3.29	Cleavage of supercoiled pBR322 by complex VOMAL at different concentrations in phosphate buffer pH 7.5. L1 Gene Ruler 1 kb DNA ladder, L2 DNA alone, Lanes 3-12 DNA with increasing concentration of complex: lane 3, 50 μM; lane 4, 100 μM; lane 5, 200 μM; lane 6, 300 μM; lane 7, 400 μM; lane 8, 500 μM; lane 9, 600 μM; lane 10, 700 μM; lane 11, 800 μM; lane 12, 900 μM.	98

LIST OF FIGURES

		Page
Figure 3.30(A)	Cleavage of supercoiled pBR322 by complex VO₂HPYDC at different concentrations in phosphate buffer pH 7.5. L1 Gene Ruler 1 kb DNA ladder, L2, DNA alone; L3, H ₂ O ₂ alone; L4, complex alone (6 mM); Lanes 5-12 DNA with increasing concentration of complex + H ₂ O ₂ : lane 5, 10 μM; lane 6, 50 μM; lane 7, 1 mM; lane 8, 2 mM; lane 9, 3 mM; lane 10, 4 mM; lane 11, 5 mM; lane 12, 6 mM.	99
Figure 3.30(B)	Cleavage of supercoiled pBR322 by complex VO₂HPYDC at different concentrations in phosphate buffer pH 7.5. L1 Gene Ruler 1 kb DNA ladder, L2, DNA alone; L3, H ₂ O ₂ alone; L4, complex alone (14 mM); Lanes 5-12 DNA with increasing concentration of complex + H ₂ O ₂ : lane 5, 7 mM; lane 6, 8 mM; lane 7, 9 mM; lane 8, 10 mM; lane 9, 11 mM; lane 10, 12 mM; lane 11, 13 mM; lane 12, 14 mM.	99
Figure 3.31	Cleavage of supercoiled pBR322 by NaVO ₃ at different concentrations in phosphate buffer pH 7.5. L1 Gene Ruler 1 kb DNA ladder, L2, DNA alone; L3, H ₂ O ₂ alone; L4, NaVO ₃ alone (14 mM); Lanes 5-12 DNA with increasing concentration of NaVO ₃ + H ₂ O ₂ : lane 5, 7 mM; lane 6, 8 mM; lane 7, 9 mM; lane 8, 10 mM; lane 9, 11 mM; lane 10, 12 mM; lane 11, 13 mM; lane 12, 14 mM.	101
Figure 3.32	Cleavage of supercoiled pBR322 by VOSO ₄ at different concentrations in phosphate buffer pH 7.5. L1 Gene Ruler 1 kb DNA ladder, L2 DNA alone, Lanes 3-12 DNA with increasing concentration of VOSO ₄ : lane 3, 50 μM; lane 4, 100 μM; lane 5, 200 μM; lane 6, 300 μM; lane 7, 400 μM; lane 8, 500 μM; lane 9, 600 μM; lane 10, 700 μM; lane 11, 800 μM; lane 12, 900 μM.	102
Figure 3.33	Effect of various scavengers on the cleavage of pBR322 by 2 mM complex VO₂PP . Lane 1, Gene Ruler 1 kb DNA ladder; Lane 2, DNA alone; Lane 3, DNA + 2 mM complex VO₂PP + H ₂ O ₂ . Lanes 4 – 12 involves reaction of 2 mM complex VO₂PP + H ₂ O ₂ with DNA in presence of various scavengers; lane 4, t-butyl alcohol (1 M); lane 5, 1 mM Mannitol; lane 6, DMSO (1 M); lane 7, 1 mM NaN ₃ ; lane 8, 10 mM NaN ₃ ; lane 9, 20 mM NaN ₃ ; lane 10, 30 mM NaN ₃ ; lane 11, 50 mM NaN ₃ ; lane 12, 100 mM NaN ₃ .	104
Figure 3.34	Effect of various scavengers on the cleavage of pBR322 by 6 mM complex VO₂GLY . Lane 1, Gene Ruler 1 kb DNA ladder; Lane 2, DNA alone; Lane 3, DNA + 6 mM complex VO₂GLY + H ₂ O ₂ . Lanes 4 – 12 involves reaction of 6 mM complex VO₂GLY + H ₂ O ₂ with DNA in presence of various scavengers; lane 4, t-butyl alcohol (1 M); lane 5, 1 mM Mannitol; lane 6, DMSO (1 M); lane 7, 1 mM NaN ₃ ; lane 8, 10 mM NaN ₃ ; lane 9, 20 mM NaN ₃ ; lane 10, 30 mM NaN ₃ ; lane 11, 50 mM NaN ₃ ; lane 12, 100 mM NaN ₃ .	104

LIST OF FIGURES

		Page
Figure 3.35	Effect of various scavengers on the cleavage of pBR322 by 7 mM complex VO₂HPYDC . Lane 1, Gene Ruler 1 kb DNA ladder; Lane 2, DNA alone; Lane 3, DNA + 7 mM complex VO₂HPYDC + H ₂ O ₂ . Lanes 4 – 12 involves reaction of 7 mM complex VO₂HPYDC + H ₂ O ₂ with DNA in presence of various scavengers; lane 4, t-butyl alcohol (1 M); lane 5, 1 mM Mannitol; lane 6, DMSO (1 M); lane 7, 1 mM NaN ₃ ; lane 8, 10 mM NaN ₃ ; lane 9, 20 mM NaN ₃ ; lane 10, 30 mM NaN ₃ ; lane 11, 50 mM NaN ₃ ; lane 12, 100 mM NaN ₃ .	105
Figure 3.36	Effect of various scavengers on the cleavage of pBR322 by 200 μM complex VOPYDC . Lane 1, Gene Ruler 1 kb DNA ladder; Lane 2, DNA alone; Lane 3, DNA + 200 μM complex VOPYDC . Lanes 4 – 12 involves reaction of 200 μM complex VOPYDC with DNA in presence of various scavengers; lane 4, t-butyl alcohol (1 M); lane 5, 1 mM Mannitol; lane 6, DMSO (1 M); lane 7, 1 mM NaN ₃ ; lane 8, 10 mM NaN ₃ ; lane 9, 20 mM NaN ₃ ; lane 10, 30 mM NaN ₃ ; lane 11, 50 mM NaN ₃ ; lane 12, 100 mM NaN ₃ .	105
Figure 3.37	Effect of various scavengers on the cleavage of pBR322 by 400 μM complex VOMAL . Lane 1, Gene Ruler 1 kb DNA ladder; Lane 2, DNA alone; Lane 3, DNA + 400 μM complex VOMAL . Lanes 4 – 12 involves reaction of 400 μM complex VOMAL with DNA in presence of various scavengers; lane 4, t-butyl alcohol (1 M); lane 5, 1 mM Mannitol; lane 6, DMSO (1 M); lane 7, 1 mM NaN ₃ ; lane 8, 10 mM NaN ₃ ; lane 9, 20 mM NaN ₃ ; lane 10, 30 mM NaN ₃ ; lane 11, 50 mM NaN ₃ ; lane 12, 100 mM NaN ₃ .	106
Figure 3.38	The proposed DNA cleavage mechanism of complexes VO₂PP , VO₂GLY and VO₂HPYDC in the presence of H ₂ O ₂	106
Figure 3.39	The proposed DNA cleavage mechanism of complexes VOPYDC and VOMAL in the absence of H ₂ O ₂	107
Figure 4.1	The molecular structure of complex Cu-4-Cl-2-NO₂BZO , showing 50 % probability displacement ellipsoids and the atomic numbering (Refer to the list of Publication at page 325)	118
Figure 4.2	The crystal packing of complex Cu-4-Cl-2-NO₂BZO	119
Figure 4.3	The molecular structure of complex Cu-2-Cl-4-NO₂BZO , showing 50 % probability displacement ellipsoids and the atomic numbering (Refer to the list of Publication at page 325)	121
Figure 4.4	The crystal packing of complex Cu-2-Cl-4-NO₂BZO	122

LIST OF FIGURES

		Page
Figure 4.5	The molecular structure of complex Cu-2-Cl-6-FBZO , showing 50 % probability displacement ellipsoids and the atomic numbering (Refer to the list of Publication at page 325)	124
Figure 4.6	The crystal packing of complex Cu-2-Cl-6-FBZO	125
Figure 4.7	The molecular structure of complex Cu-2-F-6-FBZO , showing 50 % probability displacement ellipsoids and the atomic numbering (Refer to the list of Publication at page 325)	127
Figure 4.8	The crystal packing of complex Cu-2-F-6-FBZO	128
Figure 4.9	The molecular structure of complex Cu-2-CIBZO , showing 50 % probability displacement ellipsoids and the atomic numbering	130
Figure 4.10	The crystal packing of complex Cu-2-CIBZO	131
Figure 4.11	The molecular structure of complex Cu-2-BrBZO , showing 50 % probability displacement ellipsoids and the atomic numbering	133
Figure 4.12	The crystal packing of complex Cu-2-BrBZO	134
Figure 4.13	The partial polymeric structure of complex CuP-5-Cl-2-NO₂BZO , showing 50 % probability displacement ellipsoids and the atomic numbering (Refer to the list of Publication at page 325)	138
Figure 4.14	The chemical structure of polymeric complex CuP-5-Cl-2-NO₂BZO	139
Figure 4.15	The crystal packing of polymeric complex CuP-5-Cl-2-NO₂BZO	140
Figure 4.16(A)	FT-IR spectrum of complex Cu-4-Cl-2-NO₂BZO	146
Figure 4.16(B)	FT-IR spectrum of 4-chloro-2-nitrobenzoic acid	146
Figure 4.17(A)	FT-IR spectrum of complex Cu-2-Cl-4-NO₂BZO	147
Figure 4.17(B)	FT-IR spectrum of 2-chloro-4-nitrobenzoic acid	147

LIST OF FIGURES

	Page
Figure 4.18(A) FT-IR spectrum of complex CuP-5-Cl-2-NO₂BZO	148
Figure 4.18(B) FT-IR spectrum of 5-chloro-2-nitrobenzoic acid	148
Figure 4.19(A) FT-IR spectrum of complex Cu-2-Cl-6-FBZO	149
Figure 4.19(B) FT-IR spectrum of 2-chloro-6-fluorobenzoic acid	149
Figure 4.20(A) FT-IR spectrum of complex Cu-2-F-6-FBZO	150
Figure 4.20(B) FT-IR spectrum of 2,6-difluorobenzoic acid	150
Figure 4.21(A) FT-IR spectrum of complex Cu-2-ClBZO	151
Figure 4.21(B) FT-IR spectrum of 2-chlorobenzoic acid	151
Figure 4.22(A) FT-IR spectrum of complex Cu-2-BrBZO	152
Figure 4.22(B) FT-IR spectrum of 2-bromobenzoic acid	152
Figure 4.23(A) UV-Vis spectrum of complex Cu-4-Cl-2-NO₂BZO ($6.00 \times 10^{-3} \text{ mol L}^{-1}$; $\lambda = 697 \text{ nm}$, $\epsilon = 56 \text{ mol}^{-1}\text{Lcm}^{-1}$)	155
Figure 4.23(B) UV-Vis spectrum of complex Cu-4-Cl-2-NO₂BZO ($1.20 \times 10^{-5} \text{ mol L}^{-1}$; $\lambda = 319 \text{ nm}$, $\epsilon = 3600 \text{ mol}^{-1}\text{Lcm}^{-1}$; $\lambda = 262 \text{ nm}$, $\epsilon = 10\,324 \text{ mol}^{-1}\text{Lcm}^{-1}$; $\lambda = 216 \text{ nm}$, $\epsilon = 30\,129 \text{ mol}^{-1}\text{Lcm}^{-1}$)	155
Figure 4.24(A) UV-Vis spectrum of complex Cu-2-Cl-4-NO₂BZO ($6.54 \times 10^{-3} \text{ mol L}^{-1}$; $\lambda = 674 \text{ nm}$, $\epsilon = 63 \text{ mol}^{-1}\text{Lcm}^{-1}$)	156
Figure 4.24(B) UV-Vis spectrum of complex Cu-2-Cl-4-NO₂BZO ($1.31 \times 10^{-5} \text{ mol L}^{-1}$; $\lambda = 275 \text{ nm}$, $\epsilon = 24\,477 \text{ mol}^{-1}\text{Lcm}^{-1}$; $\lambda = 211 \text{ nm}$, $\epsilon = 42\,468 \text{ mol}^{-1}\text{Lcm}^{-1}$)	156
Figure 4.25(A) UV-Vis spectrum of complex CuP-5-Cl-2-NO₂BZO ($5.90 \times 10^{-3} \text{ mol L}^{-1}$; $\lambda = 662 \text{ nm}$, $\epsilon = 60 \text{ mol}^{-1}\text{Lcm}^{-1}$)	157
Figure 4.25(B) UV-Vis spectrum of complex CuP-5-Cl-2-NO₂BZO ($1.18 \times 10^{-5} \text{ mol L}^{-1}$; $\lambda = 274 \text{ nm}$, $\epsilon = 26\,555 \text{ mol}^{-1}\text{Lcm}^{-1}$; $\lambda = 211 \text{ nm}$, $\epsilon = 43\,376 \text{ mol}^{-1}\text{Lcm}^{-1}$)	157

LIST OF FIGURES

		Page
Figure 4.26(A)	UV-Vis spectrum of complex Cu-2-Cl-6-FBZO ($6.33 \times 10^{-3} \text{ mol L}^{-1}$; $\lambda = 735 \text{ nm}$, $\epsilon = 57 \text{ mol}^{-1}\text{Lcm}^{-1}$)	158
Figure 4.26(B)	UV-Vis spectrum of complex Cu-2-Cl-6-FBZO ($1.26 \times 10^{-5} \text{ mol L}^{-1}$; $\lambda = 264 \text{ nm}$, $\epsilon = 9920 \text{ mol}^{-1}\text{Lcm}^{-1}$; $\lambda = 212 \text{ nm}$, $\epsilon = 42\,285 \text{ mol}^{-1}\text{Lcm}^{-1}$)	158
Figure 4.27(A)	UV-Vis spectrum of complex Cu-2-F-6-FBZO ($4.27 \times 10^{-3} \text{ mol L}^{-1}$; $\lambda = 692 \text{ nm}$, $\epsilon = 69 \text{ mol}^{-1}\text{Lcm}^{-1}$)	159
Figure 4.27(B)	UV-Vis spectrum of complex Cu-2-F-6-FBZO ($4.27 \times 10^{-6} \text{ mol L}^{-1}$; $\lambda = 264 \text{ nm}$, $\epsilon = 10\,009 \text{ mol}^{-1}\text{Lcm}^{-1}$; $\lambda = 210 \text{ nm}$, $\epsilon = 45\,380 \text{ mol}^{-1}\text{Lcm}^{-1}$)	159
Figure 4.28(A)	UV-Vis spectrum of complex Cu-2-CIBZO ($5.81 \times 10^{-3} \text{ mol L}^{-1}$; $\lambda = 731 \text{ nm}$, $\epsilon = 65 \text{ mol}^{-1}\text{Lcm}^{-1}$)	160
Figure 4.28(B)	UV-Vis spectrum of complex Cu-2-CIBZO ($1.16 \times 10^{-5} \text{ mol L}^{-1}$; $\lambda = 270 \text{ nm}$, $\epsilon = 9526 \text{ mol}^{-1}\text{Lcm}^{-1}$; $\lambda = 211 \text{ nm}$, $\epsilon = 47\,783 \text{ mol}^{-1}\text{Lcm}^{-1}$)	160
Figure 4.29(A)	UV-Vis spectrum of complex Cu-2-BrBZO ($4.39 \times 10^{-3} \text{ mol L}^{-1}$; $\lambda = 739 \text{ nm}$, $\epsilon = 55 \text{ mol}^{-1}\text{Lcm}^{-1}$)	161
Figure 4.29(B)	UV-Vis spectrum of complex Cu-2-BrBZO ($1.01 \times 10^{-5} \text{ mol L}^{-1}$; $\lambda = 256 \text{ nm}$, $\epsilon = 16\,300 \text{ mol}^{-1}\text{Lcm}^{-1}$; $\lambda = 211 \text{ nm}$, $\epsilon = 45\,575 \text{ mol}^{-1}\text{Lcm}^{-1}$)	161
Figure 4.30	UV-Vis spectrum of CuCl_2 (0.022 mol L^{-1} ; $\lambda = 758 \text{ nm}$, $\epsilon = 25 \text{ mol}^{-1}\text{Lcm}^{-1}$)	162
Figure 4.31	UV-Vis spectrum of CuSO_4 (0.022 mol L^{-1} ; $\lambda = 768 \text{ nm}$, $\epsilon = 22 \text{ mol}^{-1}\text{Lcm}^{-1}$)	162
Figure 4.32(A)	Cyclic voltammogram of complex Cu-4-Cl-2-NO₂BZO ; Epa = anodic oxidation peak, Epc = cathodic reduction peak	165
Figure 4.32(B)	Cyclic voltammogram of complex Cu-2-Cl-4-NO₂BZO ; Epa = anodic oxidation peak, Epc = cathodic reduction peak	165

LIST OF FIGURES

		Page
Figure 4.32(C)	Cyclic voltammogram of complex CuP-5-Cl-2-NO₂BZO ; Epa = anodic oxidation peak, Epc = cathodic reduction peak	166
Figure 4.32(D)	Cyclic voltammogram of complex Cu-2-Cl-6-FBZO ; Epa = anodic oxidation peak, Epc = cathodic reduction peak	166
Figure 4.32(E)	Cyclic voltammogram of complex Cu-2-F-6-FBZO ; Epa = anodic oxidation peak, Epc = cathodic reduction peak	167
Figure 4.32(F)	Cyclic voltammogram of complex Cu-2-ClBZO ; Epa = anodic oxidation peak, Epc = cathodic reduction peak	167
Figure 4.32(G)	Cyclic voltammogram of complex Cu-2-BrBZO ; Epa = anodic oxidation peak, Epc = cathodic reduction peak	168
Figure 4.33	Cleavage of supercoiled pBR322 by complex Cu-4-Cl-2-NO₂BZO at different concentrations in TN buffer pH 7.5. L1 Gene Ruler 1 kb DNA ladder, L2 DNA alone, L3 DNA + H ₂ O ₂ alone, L4 DNA + 40 μM complex Cu-4-Cl-2-NO₂BZO alone (without H ₂ O ₂). Lanes 5-12 DNA with increasing concentration of complex Cu-4-Cl-2-NO₂BZO + H ₂ O ₂ : lane 5, 5 μM; lane 6, 10 μM; lane 7, 15 μM; lane 8, 20 μM; lane 9, 25 μM; lane 10, 30 μM; lane 11, 35 μM; lane 12, 40 μM.	169
Figure 4.34	Cleavage of supercoiled pBR322 by complex Cu-2-Cl-4-NO₂BZO at different concentrations in TN buffer pH 7.5. L1 Gene Ruler 1 kb DNA ladder, L2 DNA alone, L3 DNA + H ₂ O ₂ alone, L4 DNA + 40 μM complex Cu-2-Cl-4-NO₂BZO alone (without H ₂ O ₂). Lanes 5-12 DNA with increasing concentration of complex Cu-2-Cl-4-NO₂BZO + H ₂ O ₂ : lane 5, 5 μM; lane 6, 10 μM; lane 7, 15 μM; lane 8, 20 μM; lane 9, 25 μM; lane 10, 30 μM; lane 11, 35 μM; lane 12, 40 μM.	170
Figure 4.35	Cleavage of supercoiled pBR322 by complex CuP-5-Cl-2-NO₂BZO at different concentrations in TN buffer pH 7.5. L1 Gene Ruler 1 kb DNA ladder, L2 DNA alone, L3 DNA + H ₂ O ₂ alone, L4 DNA + 40 μM complex CuP-5-Cl-2-NO₂BZO alone (without H ₂ O ₂). Lanes 5-12 DNA with increasing concentration of complex CuP-5-Cl-2-NO₂BZO + H ₂ O ₂ : lane 5, 5 μM; lane 6, 10 μM; lane 7, 15 μM; lane 8, 20 μM; lane 9, 25 μM; lane 10, 30 μM; lane 11, 35 μM; lane 12, 40 μM.	171
Figure 4.36	Cleavage of supercoiled pBR322 by complex Cu-2-Cl-6-FBZO at different concentrations in TN buffer pH 7.5. L1 Gene Ruler 1 kb DNA ladder, L2 DNA alone, L3 DNA + H ₂ O ₂ alone, L4 DNA + 40 μM complex Cu-2-Cl-6-FBZO alone (without H ₂ O ₂). Lanes 5-12 DNA with increasing concentration of complex Cu-2-Cl-6-FBZO + H ₂ O ₂ : lane 5, 5 μM; lane 6, 10 μM; lane 7, 15 μM; lane 8, 20 μM; lane 9, 25 μM; lane 10, 30 μM; lane 11, 35 μM; lane 12, 40 μM.	172

LIST OF FIGURES

		Page
Figure 4.37	Cleavage of supercoiled pBR322 by complex Cu-2-F-6-FBZO at different concentrations in TN buffer pH 7.5. L1 Gene Ruler 1 kb DNA ladder, L2 DNA alone, L3 DNA + H ₂ O ₂ alone, L4 DNA + 40 μM complex Cu-2-F-6-FBZO alone (without H ₂ O ₂). Lanes 5-12 DNA with increasing concentration of complex Cu-2-F-6-FBZO + H ₂ O ₂ : lane 5, 5 μM; lane 6, 10 μM; lane 7, 15 μM; lane 8, 20 μM; lane 9, 25 μM; lane 10, 30 μM; lane 11, 35 μM; lane 12, 40 μM.	173
Figure 4.38	Cleavage of supercoiled pBR322 by complex Cu-2-CIBZO at different concentrations in TN buffer pH 7.5. L1 Gene Ruler 1 kb DNA ladder, L2 DNA alone, L3 DNA + H ₂ O ₂ alone, L4 DNA + 40 μM complex Cu-2-CIBZO alone (without H ₂ O ₂). Lanes 5-12 DNA with increasing concentration of complex Cu-2-CIBZO + H ₂ O ₂ : lane 5, 5 μM; lane 6, 10 μM; lane 7, 15 μM; lane 8, 20 μM; lane 9, 25 μM; lane 10, 30 μM; lane 11, 35 μM; lane 12, 40 μM.	174
Figure 4.39	Cleavage of supercoiled pBR322 by complex Cu-2-BrBZO at different concentrations in TN buffer pH 7.5. L1 Gene Ruler 1 kb DNA ladder, L2 DNA alone, L3 DNA + H ₂ O ₂ alone, L4 DNA + 40 μM complex Cu-2-BrBZO alone (without H ₂ O ₂). Lanes 5-12 DNA with increasing concentration of complex Cu-2-BrBZO + H ₂ O ₂ : lane 5, 5 μM; lane 6, 10 μM; lane 7, 15 μM; lane 8, 20 μM; lane 9, 25 μM; lane 10, 30 μM; lane 11, 35 μM; lane 12, 40 μM.	175
Figure 4.40	Cleavage of supercoiled pBR322 by CuCl ₂ at different concentrations in TN buffer pH 7.5. L1 Gene Ruler 1 kb DNA ladder, L2 DNA alone, L3 DNA + H ₂ O ₂ alone, L4 DNA + 40 μM CuCl ₂ alone (without H ₂ O ₂). Lanes 5-12 DNA with increasing concentration of CuCl ₂ + H ₂ O ₂ : lane 5, 5 μM; lane 6, 10 μM; lane 7, 15 μM; lane 8, 20 μM; lane 9, 25 μM; lane 10, 30 μM; lane 11, 35 μM; lane 12, 40 μM.	177
Figure 4.41	Cleavage of supercoiled pBR322 by CuSO ₄ at different concentrations in TN buffer pH 7.5. L1 Gene Ruler 1 kb DNA ladder, L2 DNA alone, L3 DNA + H ₂ O ₂ alone, L4 DNA + 40 μM CuSO ₄ alone (without H ₂ O ₂). Lanes 5-12 DNA with increasing concentration of CuSO ₄ + H ₂ O ₂ : lane 5, 5 μM; lane 6, 10 μM; lane 7, 15 μM; lane 8, 20 μM; lane 9, 25 μM; lane 10, 30 μM; lane 11, 35 μM; lane 12, 40 μM.	178
Figure 4.42	Effect of various scavengers on the cleavage of pBR322 by 40 μM complex Cu-4-Cl-2-NO₂BZO Lane 1, Gene Ruler 1 kb DNA ladder; lane 2, DNA alone; lane 3, DNA + 40 μM of complex Cu-4-Cl-2-NO₂BZO + H ₂ O ₂ . Lanes 4 – 12 involves reaction of 40 μM complex Cu-4-Cl-2-NO₂BZO + H ₂ O ₂ with DNA in presence of various scavengers; lane 4, t-butyl alcohol (1 M); lane 5, 1 mM Mannitol; lane 6, DMSO (1 M); lane 7, 1 mM NaN ₃ ; lane 8, 10 mM NaN ₃ ; lane 9, 20 mM NaN ₃ ; lane 10, 30 mM NaN ₃ ; lane 11, 40 mM NaN ₃ ; lane 12, 50 mM NaN ₃ .	180

LIST OF FIGURES

	Page
Figure 4.43	Effect of various scavengers on the cleavage of pBR322 by 40 μ M complex Cu-2-Cl-4-NO₂BZO Lane 1, Gene Ruler 1 kb DNA ladder; lane 2, DNA alone; lane 3, DNA + 40 μ M of complex Cu-2-Cl-4-NO₂BZO + H ₂ O ₂ . Lanes 4 – 12 involves reaction of 40 μ M complex Cu-2-Cl-4-NO₂BZO + H ₂ O ₂ with DNA in presence of various scavengers; lane 4, t-butyl alcohol (1 M); lane 5, 1 mM Mannitol; lane 6, DMSO (1 M); lane 7, 1 mM NaN ₃ ; lane 8, 10 mM NaN ₃ ; lane 9, 20 mM NaN ₃ ; lane 10, 30 mM NaN ₃ ; lane 11, 40 mM NaN ₃ ; lane 12, 50 mM NaN ₃ . 180
Figure 4.44	Effect of various scavengers on the cleavage of pBR322 by 40 μ M complex CuP-5-Cl-2-NO₂BZO Lane 1, Gene Ruler 1 kb DNA ladder; lane 2, DNA alone; lane 3, DNA + 40 μ M of complex CuP-5-Cl-2-NO₂BZO + H ₂ O ₂ . Lanes 4 – 12 involves reaction of 40 μ M complex CuP-5-Cl-2-NO₂BZO + H ₂ O ₂ with DNA in presence of various scavengers; lane 4, t-butyl alcohol (1 M); lane 5, 1 mM Mannitol; lane 6, DMSO (1 M); lane 7, 1 mM NaN ₃ ; lane 8, 10 mM NaN ₃ ; lane 9, 20 mM NaN ₃ ; lane 10, 30 mM NaN ₃ ; lane 11, 40 mM NaN ₃ ; lane 12, 50 mM NaN ₃ . 181
Figure 4.45	Effect of various scavengers on the cleavage of pBR322 by 40 μ M complex Cu-2-Cl-6-FBZO Lane 1, Gene Ruler 1 kb DNA ladder; lane 2, DNA alone; lane 3, DNA + 40 μ M of complex Cu-2-Cl-6-FBZO + H ₂ O ₂ . Lanes 4 – 12 involves reaction of 40 μ M complex Cu-2-Cl-6-FBZO + H ₂ O ₂ with DNA in presence of various scavengers; lane 4, t-butyl alcohol (1 M); lane 5, 1 mM Mannitol; lane 6, DMSO (1 M); lane 7, 1 mM NaN ₃ ; lane 8, 10 mM NaN ₃ ; lane 9, 20 mM NaN ₃ ; lane 10, 30 mM NaN ₃ ; lane 11, 40 mM NaN ₃ ; lane 12, 50 mM NaN ₃ . 181
Figure 4.46	Effect of various scavengers on the cleavage of pBR322 by 40 μ M complex Cu-2-F-6-FBZO Lane 1, Gene Ruler 1 kb DNA ladder; lane 2, DNA alone; lane 3, DNA + 40 μ M of complex Cu-2-F-6-FBZO + H ₂ O ₂ . Lanes 4 – 12 involves reaction of 40 μ M complex Cu-2-F-6-FBZO + H ₂ O ₂ with DNA in presence of various scavengers; lane 4, t-butyl alcohol (1 M); lane 5, 1 mM Mannitol; lane 6, DMSO (1 M); lane 7, 1 mM NaN ₃ ; lane 8, 10 mM NaN ₃ ; lane 9, 20 mM NaN ₃ ; lane 10, 30 mM NaN ₃ ; lane 11, 40 mM NaN ₃ ; lane 12, 50 mM NaN ₃ . 182
Figure 4.47	Effect of various scavengers on the cleavage of pBR322 by 40 μ M complex Cu-2-CIBZO Lane 1, Gene Ruler 1 kb DNA ladder; lane 2, DNA alone; lane 3, DNA + 40 μ M of complex Cu-2-CIBZO + H ₂ O ₂ . Lanes 4 – 12 involves reaction of 40 μ M complex Cu-2-CIBZO + H ₂ O ₂ with DNA in presence of various scavengers; lane 4, t-butyl alcohol (1 M); lane 5, 1 mM Mannitol; lane 6, DMSO (1 M); lane 7, 1 mM NaN ₃ ; lane 8, 10 mM NaN ₃ ; lane 9, 20 mM NaN ₃ ; lane 10, 30 mM NaN ₃ ; lane 11, 40 mM NaN ₃ ; lane 12, 50 mM NaN ₃ . 182

LIST OF FIGURES

		Page
Figure 4.48	Effect of various scavengers on the cleavage of pBR322 by 40 μ M complex Cu-2-BrBZO Lane 1, Gene Ruler 1 kb DNA ladder; lane 2, DNA alone; lane 3, DNA + 40 μ M of complex Cu-2-BrBZO + H ₂ O ₂ . Lanes 4 – 12 involves reaction of 40 μ M complex Cu-2-BrBZO + H ₂ O ₂ with DNA in presence of various scavengers; lane 4, t-butyl alcohol (1 M); lane 5, 1 mM Mannitol; lane 6, DMSO (1 M); lane 7, 1 mM NaN ₃ , lane 8, 10 mM NaN ₃ , lane 9, 20 mM NaN ₃ , lane 10, 30 mM NaN ₃ , lane 11, 40 mM NaN ₃ , lane 12, 50 mM NaN ₃ .	183
Figure 4.49	The proposed DNA cleavage mechanism of complexes Cu-4-Cl-2-NO₂BZO , Cu-2-Cl-4-NO₂BZO , CuP-5-Cl-2-NO₂BZO , Cu-2-Cl-6-FBZO , Cu-2-F-6-FBZO , Cu-2-CIBZO and Cu-2-BrBZO in the presence of H ₂ O ₂	183
Figure 5.1	The partial polymeric structure of complex MnP-4-Cl-2-NO₂BZO , showing 50 % probability displacement ellipsoids and the atomic numbering	195
Figure 5.2	The crystal packing of polymeric complex MnP-4-Cl-2-NO₂BZO	196
Figure 5.3	The partial polymeric structure of complex MnP-3-NO₂-5-NO₂BZO , showing 50 % probability displacement ellipsoids and the atomic numbering	198
Figure 5.4	The crystal packing of polymeric complex MnP-3-NO₂-5-NO₂BZO	198
Figure 5.5	The molecular structure of complex Mn-4-NO₂BZO , showing 50 % probability displacement ellipsoids and the atomic numbering	200
Figure 5.6	The crystal packing of complex Mn-4-NO₂BZO	201
Figure 5.7	The partial polymeric structure of complex MnP-4-NH₂BZO , showing 50 % probability displacement ellipsoids and the atomic numbering	205
Figure 5.8	The crystal packing of polymeric complex MnP-4-NH₂BZO	206
Figure 5.9	The partial polymeric structure of complex MnP-4-FBZO , showing 50 % probability displacement ellipsoids and the atomic numbering	210

LIST OF FIGURES

		Page
Figure 5.10	The crystal packing of polymeric complex MnP-4-FBZO	211
Figure 5.11	The partial polymeric structure of complex MnPGLY , showing 50 % probability displacement ellipsoids and the atomic numbering	215
Figure 5.12	The crystal packing of polymeric complex MnPGLY	216
Figure 5.13	FT-IR spectrum of complex MnP-4-Cl-2-NO₂BZO	224
Figure 5.14(A)	FT-IR spectrum of complex MnP-3-NO₂-5-NO₂BZO	224
Figure 5.14(B)	FT-IR spectrum of 3,5-dinitrobenzoic acid	225
Figure 5.15(A)	FT-IR spectrum of complex Mn-4-NO₂BZO	225
Figure 5.15(B)	FT-IR spectrum of 4-nitrobenzoic acid	226
Figure 5.16(A)	FT-IR spectrum of complex MnP-4-NH₂BZO	226
Figure 5.16(B)	FT-IR spectrum of 4-aminobenzoic acid	227
Figure 5.17(A)	FT-IR spectrum of complex MnP-4-FBZO	227
Figure 5.17(B)	FT-IR spectrum of 4-flouorobenzoic acid	228
Figure 5.18	Postulated structure of partial polymeric complex MnP-4-CIBZO	228
Figure 5.19(A)	FT-IR spectrum of complex MnP-4-CIBZO	229
Figure 5.19(B)	FT-IR spectrum of 4-chlorobenzoic acid	229
Figure 5.20	FT-IR spectrum of complex MnPGLY	230
Figure 5.21	Chemical structure of complex MnPyr [73]	230
Figure 5.22	FT-IR spectrum of complex MnPyr	231

LIST OF FIGURES

	Page
Figure 5.23(A) UV-Vis spectrum of complex MnP-4-Cl-2-NO₂BZO ($8.37 \times 10^{-3} \text{ mol L}^{-1}$)	234
Figure 5.23(B) UV-Vis spectrum of complex MnP-4-Cl-2-NO₂BZO ($2.00 \times 10^{-5} \text{ mol L}^{-1}$; $\lambda = 318 \text{ nm}$, $\epsilon = 4127 \text{ mol}^{-1}\text{Lcm}^{-1}$; $\lambda = 262 \text{ nm}$, $\epsilon = 11122 \text{ mol}^{-1}\text{Lcm}^{-1}$; $\lambda = 214 \text{ nm}$, $\epsilon = 41036 \text{ mol}^{-1}\text{Lcm}^{-1}$)	234
Figure 5.24(A) UV-Vis spectrum of complex MnP-3-NO₂-5-NO₂BZO ($5.22 \times 10^{-3} \text{ mol L}^{-1}$)	235
Figure 5.24(B) UV-Vis spectrum of complex MnP-3-NO₂-5-NO₂BZO ($2.08 \times 10^{-5} \text{ mol L}^{-1}$; $\lambda = 238 \text{ nm}$, $\epsilon = 32169 \text{ mol}^{-1}\text{Lcm}^{-1}$; $\lambda = 212 \text{ nm}$, $\epsilon = 45175 \text{ mol}^{-1}\text{Lcm}^{-1}$)	235
Figure 5.25(A) UV-Vis spectrum of complex Mn-4-NO₂BZO ($6.45 \times 10^{-3} \text{ mol L}^{-1}$)	236
Figure 5.25(B) UV-Vis spectrum of complex Mn-4-NO₂BZO ($2.57 \times 10^{-5} \text{ mol L}^{-1}$; $\lambda = 273 \text{ nm}$, $\epsilon = 19411 \text{ mol}^{-1}\text{Lcm}^{-1}$; $\lambda = 210 \text{ nm}$, $\epsilon = 18785 \text{ mol}^{-1}\text{Lcm}^{-1}$)	236
Figure 5.26(A) UV-Vis spectrum of complex MnP-4-NH₂BZO (0.010 mol L^{-1})	237
Figure 5.26(B) UV-Vis spectrum of complex MnP-4-NH₂BZO ($8.23 \times 10^{-6} \text{ mol L}^{-1}$; $\lambda = 265 \text{ nm}$, $\epsilon = 30469 \text{ mol}^{-1}\text{Lcm}^{-1}$; $\lambda = 210 \text{ nm}$, $\epsilon = 36701 \text{ mol}^{-1}\text{Lcm}^{-1}$)	237
Figure 5.27(A) UV-Vis spectrum of complex MnP-4-FBZO ($6.26 \times 10^{-3} \text{ mol L}^{-1}$)	238
Figure 5.27(B) UV-Vis spectrum of complex MnP-4-FBZO ($2.50 \times 10^{-5} \text{ mol L}^{-1}$; $\lambda = 223 \text{ nm}$, $\epsilon = 18\,000 \text{ mol}^{-1}\text{Lcm}^{-1}$)	238
Figure 5.28(A) UV-Vis spectrum of complex MnP-4-CIBZO ($5.82 \times 10^{-3} \text{ mol L}^{-1}$)	239
Figure 5.28(B) UV-Vis spectrum of complex MnP-4-CIBZO ($2.32 \times 10^{-5} \text{ mol L}^{-1}$; $\lambda = 225 \text{ nm}$, $\epsilon = 17\,835 \text{ mol}^{-1}\text{Lcm}^{-1}$)	239

LIST OF FIGURES

		Page
Figure 5.29(A)	UV-Vis spectrum of complex MnPGLY (0.015 mol L^{-1})	240
Figure 5.29(B)	UV-Vis spectrum of complex MnPGLY ($3.05 \times 10^{-3} \text{ mol L}^{-1}$; $A = 212 \text{ nm}$, $\epsilon = 156 \text{ mol}^{-1}\text{Lcm}^{-1}$)	240
Figure 5.30(A)	UV-Vis spectrum of complex MnPyr (0.012 mol L^{-1})	241
Figure 5.30(B)	UV-Vis spectrum of complex MnPyr ($4.65 \times 10^{-5} \text{ mol L}^{-1}$; $A = 262 \text{ nm}$, $\epsilon = 8699 \text{ mol}^{-1}\text{Lcm}^{-1}$; $A = 213 \text{ nm}$, $\epsilon = 18147 \text{ mol}^{-1}\text{Lcm}^{-1}$)	241
Figure 5.31	UV-Vis spectrum of complex MnCl₂ (0.031 mol L^{-1} ; $A = 211 \text{ nm}$; $\epsilon = 11 \text{ mol}^{-1}\text{Lcm}^{-1}$)	242
Figure 5.32(A)	Cyclic voltammogram of complex MnP-4-Cl-2-NO₂BZO ; E _{pa} = anodic oxidation peak, E _{pc} = cathodic reduction peak	245
Figure 5.32(B)	Cyclic voltammogram of complex MnP-3-NO₂-5-NO₂BZO ; E _{pa} = anodic oxidation peak, E _{pc} = cathodic reduction peak	245
Figure 5.32(C)	Cyclic voltammogram of complex Mn-4-NO₂BZO ; E _{pa} = anodic oxidation peak, E _{pc} = cathodic reduction peak	246
Figure 5.32(D)	Cyclic voltammogram of complex MnP-4-NH₂BZO ; E _{pa} = anodic oxidation peak, E _{pc} = cathodic reduction peak	246
Figure 5.32(E)	Cyclic voltammogram of complex MnP-4-FBZO ; E _{pa} = anodic oxidation peak, E _{pc} = cathodic reduction peak	247
Figure 5.32(F)	Cyclic voltammogram of complex MnP-4-CIBZO ; E _{pa} = anodic oxidation peak, E _{pc} = cathodic reduction peak	247
Figure 5.32(G)	Cyclic voltammogram of complex MnPGLY ; E _{pa} = anodic oxidation peak, E _{pc} = cathodic reduction peak	248
Figure 5.32(H)	Cyclic voltammogram of complex MnPyr ; E _{pa} = anodic oxidation peak, E _{pc} = cathodic reduction peak	248

LIST OF FIGURES

	Page	
Figure 5.33	Cleavage of supercoiled pBR322 by complex MnP-4-CI-2-NO₂BZO at different concentrations in TN buffer pH 7.5. L1 Gene Ruler 1 kb DNA ladder; L2, DNA alone; L3, DNA + H ₂ O ₂ alone; L4, DNA + complex alone (80 μM). Lanes 5-12 DNA with increasing concentration of complex MnP-4-CI-2-NO₂BZO + H ₂ O ₂ : lane 5, 10 μM; lane 6, 20 μM; lane 7, 30 μM; lane 8, 40 μM; lane 9, 50 μM; lane 10, 60 μM; lane 11, 70 μM; lane 12, 80 μM.	250
Figure 5.34	Cleavage of supercoiled pBR322 by complex MnP-3-NO₂-5-NO₂BZO at different concentrations in TN buffer pH 7.5. L1 Gene Ruler 1 kb DNA ladder; L2, DNA alone; L3, DNA + H ₂ O ₂ alone; L4, DNA + complex alone (160 μM). Lanes 5-12 DNA with increasing concentration of complex MnP-3-NO₂-5-NO₂BZO + H ₂ O ₂ : lane 5, 80 μM; lane 6, 100 μM; lane 7, 110 μM; lane 8, 120 μM; lane 9, 130 μM; lane 10, 140 μM; lane 11, 150 μM; lane 12, 160 μM.	251
Figure 5.35	Cleavage of supercoiled pBR322 by complex Mn-4-NO₂BZO at different concentrations in TN buffer pH 7.5. L1 Gene Ruler 1 kb DNA ladder; L2, DNA alone; L3, DNA + H ₂ O ₂ alone; L4, DNA + complex alone (160 μM). Lanes 5-12 DNA with increasing concentration of complex Mn-4-NO₂BZO + H ₂ O ₂ : lane 5, 80 μM; lane 6, 100 μM; lane 7, 110 μM; lane 8, 120 μM; lane 9, 130 μM; lane 10, 140 μM; lane 11, 150 μM; lane 12, 160 μM.	252
Figure 5.36	Cleavage of supercoiled pBR322 by complex MnP-4-NH₂BZO at different concentrations in TN buffer pH 7.5. L1 Gene Ruler 1 kb DNA ladder; L2, DNA alone; L3, DNA + H ₂ O ₂ alone; L4, DNA + complex alone (160 μM). Lanes 5-12 DNA with increasing concentration of complex MnP-4-NH₂BZO + H ₂ O ₂ : lane 5, 80 μM; lane 6, 100 μM; lane 7, 110 μM; lane 8, 120 μM; lane 9, 130 μM; lane 10, 140 μM; lane 11, 150 μM; lane 12, 160 μM.	253
Figure 5.37	Cleavage of supercoiled pBR322 by complex MnP-4-FBZO at different concentrations in TN buffer pH 7.5. L1 Gene Ruler 1 kb DNA ladder; L2, DNA alone; L3, DNA + H ₂ O ₂ alone; L4 DNA + complex alone (80 μM). Lanes 5-12 DNA with increasing concentration of complex MnP-4-FBZO + H ₂ O ₂ : lane 5, 10 μM; lane 6, 20 μM; lane 7, 30 μM; lane 8, 40 μM; lane 9, 50 μM; lane 10, 60 μM; lane 11, 70 μM; lane 12, 80 μM.	254
Figure 5.38	Cleavage of supercoiled pBR322 by complex MnP-4-CIBZO at different concentrations in TN buffer pH 7.5. L1 Gene Ruler 1 kb DNA ladder; L2, DNA alone; L3, DNA + H ₂ O ₂ alone; L4 DNA + complex alone (80 μM). Lanes 5-12 DNA with increasing concentration of complex MnP-4-CIBZO + H ₂ O ₂ : lane 5, 10 μM; lane 6, 20 μM; lane 7, 30 μM; lane 8, 40 μM; lane 9, 50 μM; lane 10, 60 μM; lane 11, 70 μM; lane 12, 80 μM.	255

LIST OF FIGURES

		Page
Figure 5.39	Cleavage of supercoiled pBR322 by complex MnPGLY at different concentrations in TN buffer pH 7.5. L1 Gene Ruler 1 kb DNA ladder; L2, DNA alone; L3, DNA + H ₂ O ₂ alone; L4, DNA + complex alone (80 μM). Lanes 5-12 DNA with increasing concentration of complex MnPGLY + H ₂ O ₂ : lane 5, 10 μM; lane 6, 20 μM; lane 7, 30 μM; lane 8, 40 μM; lane 9, 50 μM; lane 10, 60 μM; lane 11, 70 μM; lane 12, 80 μM.	256
Figure 5.40	Cleavage of supercoiled pBR322 by complex MnPyr at different concentrations in TN buffer pH 7.5. L1 Gene Ruler 1 kb DNA ladder; L2, DNA alone; L3, DNA + H ₂ O ₂ alone; L4, DNA + complex alone (80 μM). Lanes 5-12 DNA with increasing concentration of complex MnPyr + H ₂ O ₂ : lane 5, 10 μM; lane 6, 20 μM; lane 7, 30 μM; lane 8, 40 μM; lane 9, 50 μM; lane 10, 60 μM; lane 11, 70 μM; lane 12, 80 μM.	257
Figure 5.41	Cleavage of supercoiled pBR322 by MnCl ₂ at different concentrations in TN buffer pH 7.5. L1 Gene Ruler 1 kb DNA ladder; L2, DNA alone; L3, DNA + H ₂ O ₂ alone; L4, DNA + MnCl ₂ alone (160 μM); lane 5, 80 μM; lane 6, 100 μM; lane 7, 110 μM; lane 8, 120 μM; lane 9, 130 μM; lane 10, 140 μM; lane 11, 150 μM; lane 12, 160 μM	259
Figure 5.42	Effect of various scavengers on the cleavage of pBR322 by 50 μM complex MnP-4-Cl-2-NO₂BZO . Lane 1, Gene Ruler 1 kb DNA ladder; lane 2, DNA alone; lane 3, DNA + 50 μM complex MnP-4-Cl-2-NO₂BZO + H ₂ O ₂ . Lanes 4 – 12 involves reaction of 50 μM complex MnP-4-Cl-2-NO₂BZO + H ₂ O ₂ with DNA in presence of various scavengers; lane 4, t-butyl alcohol (1 M); lane 5, 1 mM Mannitol; lane 6, DMSO (1 M); lane 7, 1 mM NaN ₃ ; lane 8, 10 mM NaN ₃ ; lane 9, 20 mM NaN ₃ ; lane 10, 30 mM NaN ₃ ; lane 11, 50 mM NaN ₃ ; lane 12, 100 mM NaN ₃ .	261
Figure 5.43	Effect of various scavengers on the cleavage of pBR322 by 100 μM complex MnP-3-NO₂-5-NO₂BZO . Lane 1, Gene Ruler 1 kb DNA ladder; lane 2, DNA alone; lane 3, DNA + 100 μM complex MnP-3-NO₂-5-NO₂BZO + H ₂ O ₂ . Lanes 4 – 12 involves reaction of 100 μM complex MnP-3-NO₂-5-NO₂BZO + H ₂ O ₂ with DNA in presence of various scavengers; lane 4, t-butyl alcohol (1 M); lane 5, 1 mM Mannitol; lane 6, DMSO (1 M); lane 7, 1 mM NaN ₃ ; lane 8, 10 mM NaN ₃ ; lane 9, 20 mM NaN ₃ ; lane 10, 30 mM NaN ₃ ; lane 11, 50 mM NaN ₃ ; lane 12, 100 mM NaN ₃ .	261
Figure 5.44	Effect of various scavengers on the cleavage of pBR322 by 110 μM complex Mn-4-NO₂BZO . Lane 1, Gene Ruler 1 kb DNA ladder; lane 2, DNA alone; lane 3, DNA + 110 μM complex Mn-4-NO₂BZO + H ₂ O ₂ . Lanes 4 – 12 involves reaction of 110 μM complex Mn-4-NO₂BZO + H ₂ O ₂ with DNA in presence of various scavengers; lane 4, t-butyl alcohol (1 M); lane 5, 1 mM Mannitol; lane 6, DMSO (1 M); lane 7, 1 mM NaN ₃ ; lane 8, 10 mM NaN ₃ ; lane 9, 20 mM NaN ₃ ; lane 10, 30 mM NaN ₃ ; lane 11, 50 mM NaN ₃ ; lane 12, 100 mM NaN ₃ .	262

LIST OF FIGURES

	Page
Figure 5.45	Effect of various scavengers on the cleavage of pBR322 by 100 μ M complex MnP-4-NH₂BZO . Lane 1, Gene Ruler 1 kb DNA ladder; lane 2, DNA alone; lane 3, DNA + 100 μ M complex MnP-4-NH₂BZO + H ₂ O ₂ . Lanes 4 – 12 involves reaction of 100 μ M complex MnP-4-NH₂BZO + H ₂ O ₂ with DNA in presence of various scavengers; lane 4, t-butyl alcohol (1 M); lane 5, 1 mM Mannitol; lane 6, DMSO (1 M); lane 7, 1 mM NaN ₃ ; lane 8, 10 mM NaN ₃ ; lane 9, 20 mM NaN ₃ ; lane 10, 30 mM NaN ₃ ; lane 11, 50 mM NaN ₃ ; lane 12, 100 mM NaN ₃ . 262
Figure 5.46	Effect of various scavengers on the cleavage of pBR322 by 50 μ M complex MnP-4-FBZO . Lane 1, Gene Ruler 1 kb DNA ladder; lane 2, DNA alone; lane 3, DNA + 50 μ M complex MnP-4-FBZO + H ₂ O ₂ . Lanes 4 – 12 involves reaction of 50 μ M complex MnP-4-FBZO + H ₂ O ₂ with DNA in presence of various scavengers; lane 4, t-butyl alcohol (1 M); lane 5, 1 mM Mannitol; lane 6, DMSO (1 M); lane 7, 1 mM NaN ₃ ; lane 8, 10 mM NaN ₃ ; lane 9, 20 mM NaN ₃ ; lane 10, 30 mM NaN ₃ ; lane 11, 50 mM NaN ₃ ; lane 12, 100 mM NaN ₃ . 263
Figure 5.47	Effect of various scavengers on the cleavage of pBR322 by 60 μ M complex MnP-4-CIBZO . Lane 1, Gene Ruler 1 kb DNA ladder; lane 2, DNA alone; lane 3, DNA + 60 μ M complex MnP-4-CIBZO + H ₂ O ₂ . Lanes 4 – 12 involves reaction of 60 μ M complex MnP-4-CIBZO + H ₂ O ₂ with DNA in presence of various scavengers; lane 4, t-butyl alcohol (1 M); lane 5, 1 mM Mannitol; lane 6, DMSO (1 M); lane 7, 1 mM NaN ₃ ; lane 8, 10 mM NaN ₃ ; lane 9, 20 mM NaN ₃ ; lane 10, 30 mM NaN ₃ ; lane 11, 50 mM NaN ₃ ; lane 12, 100 mM NaN ₃ . 263
Figure 5.48	Effect of various scavengers on the cleavage of pBR322 by 60 μ M complex MnPGLY . Lane 1, Gene Ruler 1 kb DNA ladder; lane 2, DNA alone; lane 3, DNA + 60 μ M complex MnPGLY + H ₂ O ₂ . Lanes 4 – 12 involves reaction of 60 μ M complex MnPGLY + H ₂ O ₂ with DNA in presence of various scavengers; lane 4, t-butyl alcohol (1 M); lane 5, 1 mM Mannitol; lane 6, DMSO (1 M); lane 7, 1 mM NaN ₃ ; lane 8, 10 mM NaN ₃ ; lane 9, 20 mM NaN ₃ ; lane 10, 30 mM NaN ₃ ; lane 11, 50 mM NaN ₃ ; lane 12, 100 mM NaN ₃ . 264
Figure 5.49	Effect of various scavengers on the cleavage of pBR322 by 60 μ M complex MnP_{yr} . Lane 1, Gene Ruler 1 kb DNA ladder; lane 2, DNA alone; lane 3, DNA + 60 μ M complex MnP_{yr} + H ₂ O ₂ . Lanes 4 – 12 involves reaction of 60 μ M complex MnP_{yr} + H ₂ O ₂ with DNA in presence of various scavengers; lane 4, t-butyl alcohol (1 M); lane 5, 1 mM Mannitol; lane 6, DMSO (1 M); lane 7, 1 mM NaN ₃ ; lane 8, 10 mM NaN ₃ ; lane 9, 20 mM NaN ₃ ; lane 10, 30 mM NaN ₃ ; lane 11, 50 mM NaN ₃ ; lane 12, 100 mM NaN ₃ . 264
Figure 5.50	The proposed DNA cleavage mechanism of complexes MnP-4-Cl-2-NO₂BZO , MnP-3-NO₂-5-NO₂BZO , Mn-4-NO₂BZO , MnP-4-NH₂BZO , MnP-4-FBZO , MnP-4-CIBZO , MnPGLY and MnP_{yr} 265

LIST OF FIGURES

		Page
Figure 6.1	The postulated chemical structure of complexes VOPhen , VODMPhen , VODPPhen and VODMPPhen	271
Figure 6.2(A)	FT-IR spectrum of complex VOPhen	274
Figure 6.2(B)	FT-IR spectrum of 1,10-phenanthroline	274
Figure 6.3(A)	FT-IR spectrum of complex VODMPhen	275
Figure 6.3(B)	FT-IR spectrum of 2,9-dimethyl-1,10-phenanthroline	275
Figure 6.4(A)	FT-IR spectrum of complex VODPPhen	276
Figure 6.4(B)	FT-IR spectrum of 4,7-diphenyl-1,10-phenanthroline	276
Figure 6.5(A)	FT-IR spectrum of complex VODMPPhen	277
Figure 6.5(B)	FT-IR spectrum of 2,9-dimethyl-4,7-diphenyl-1,10-phenanthroline	277
Figure 6.6	Absorption spectra of complex VOPhen in the absence and in the presence of increasing amount of DNA, [complex] = 20 μM , [DNA] = 20-120 μM	281
Figure 6.7	Absorption spectra of complex VODMPhen in the absence and in the presence of increasing amount of DNA, [complex] = 20 μM , [DNA] = 20-120 μM	281
Figure 6.8	Absorption spectra of complex VODPPhen in the absence and in the presence of increasing amount of DNA, [complex] = 20 μM , [DNA] = 10-60 μM	282
Figure 6.9	Absorption spectra of complex VODMPPhen in the absence and in the presence of increasing amount of DNA, [complex] = 20 μM , [DNA] = 10-60 μM	282
Figure 6.10	Plot of $[\text{DNA}]/(\epsilon_a - \epsilon_f)$ versus [DNA] of complex VOPhen	283
Figure 6.11	Plot of $[\text{DNA}]/(\epsilon_a - \epsilon_f)$ versus [DNA] of complex VODMPhen	283
Figure 6.12	Plot of $[\text{DNA}]/(\epsilon_a - \epsilon_f)$ versus [DNA] of complex VODPPhen	284

LIST OF FIGURES

		Page
Figure 6.13	Plot of $[DNA]/(\epsilon_a - \epsilon_f)$ versus $[DNA]$ of complex VODMPPhen	284
Figure 6.14	Absorption spectra of complex VO₂PP in the absence and in the presence of increasing amount of DNA, $[complex] = 40 \mu M$, $[DNA] = 120 \mu M$ (Ratio DNA: Complex; 1:3)	287
Figure 6.15	Absorption spectra of complex Cu-2-Cl-6-FBZO in the absence and in the presence of increasing amount of DNA, $[complex] = 13 \mu M$, $[DNA] = 39 \mu M$ (Ratio DNA: Complex; 1:3)	287
Figure 6.16	Absorption spectra of complex Mn-4-NO₂BZO in the absence and in the presence of increasing amount of DNA, $[complex] = 26 \mu M$, $[DNA] = 78 \mu M$ (Ratio DNA: Complex; 1:3)	288
Figure 6.17	Effect of increasing amounts of complexes VOPhen , VODMPhen , VODPPhen and VODMPPhen on the relative viscosities of CT-DNA at $30 (\pm 0.1) ^\circ C$, $[DNA] = 200 \mu M$	289
Figure 6.18	(a) CD spectrum of CT DNA in the absence of complex ($50 \mu M$); (b) CD spectrum of CT DNA ($50 \mu M$) in the presence of complex VOPhen ($50 \mu M$); (c) CD spectrum of CT DNA ($50 \mu M$) in the presence of complex VODMPhen ($50 \mu M$)	291
Figure 6.19	Cleavage of supercoiled pBR322 by complex VOPhen at different concentrations in Tris-HCl buffer pH 7.5. L1 Gene Ruler 1 kb DNA ladder, L2 DNA alone, L3 H ₂ O ₂ alone, L4 complex VOPhen alone ($40 \mu M$). Lanes 5-12 DNA with increasing concentration of complex VOPhen + H ₂ O ₂ : lane 5, $5 \mu M$; lane 6, $10 \mu M$; lane 7, $15 \mu M$; lane 8, $20 \mu M$; lane 9, $25 \mu M$; lane 10, $30 \mu M$; lane 11, $35 \mu M$; lane 12, $40 \mu M$.	294
Figure 6.20	Cleavage of supercoiled pBR322 by complex VOPhen at different concentrations in Tris-HCl buffer pH 7.5. L1 Gene Ruler 1 kb DNA ladder, L2 DNA alone, Lanes 3-12 DNA with increasing concentration of complex VOPhen : lane 3, $50 \mu M$; lane 4, $70 \mu M$; lane 5, $100 \mu M$; lane 6, $120 \mu M$; lane 7, $140 \mu M$; lane 8, $160 \mu M$; lane 9, $180 \mu M$; lane 10, $200 \mu M$; lane 11, $220 \mu M$; lane 12, $240 \mu M$.	294
Figure 6.21	Cleavage of supercoiled pBR322 by complex VODMPhen at different concentrations in Tris-HCl buffer pH 7.5. L1 Gene Ruler 1 kb DNA ladder, L2 DNA alone, L3 H ₂ O ₂ alone, L4 complex VODMPhen alone ($240 \mu M$). Lanes 5-12 DNA with increasing concentration of complex VODMPhen + H ₂ O ₂ : lane 5, $100 \mu M$; lane 6, $120 \mu M$; lane 7, $140 \mu M$; lane 8, $160 \mu M$; lane 9, $180 \mu M$; lane 10, $200 \mu M$; lane 11, $220 \mu M$; lane 12, $240 \mu M$.	295

LIST OF FIGURES

		Page
Figure 6.22	Cleavage of supercoiled pBR322 by complex VODPPhen at different concentrations in Tris-HCl buffer pH 7.5. L1 Gene Ruler 1 kb DNA ladder, L2 DNA alone, L3 H ₂ O ₂ alone, L4 complex VODPPhen alone (40 μM). Lanes 5-12 DNA with increasing concentration of complex VODPPhen + H ₂ O ₂ : lane 5, 5 μM; lane 6, 10 μM; lane 7, 15 μM; lane 8, 20 μM; lane 9, 25 μM; lane 10, 30 μM; lane 11, 35 μM; lane 12, 40 μM.	295
Figure 6.23	Cleavage of supercoiled pBR322 by complex VODMPPhen at different concentrations in Tris-HCl buffer pH 7.5. L1 Gene Ruler 1 kb DNA ladder, L2 DNA alone, L3 H ₂ O ₂ alone, L4 complex VODMPPhen alone (240 μM). Lanes 5-12 DNA with increasing concentration of complex VODMPPhen + H ₂ O ₂ : lane 5, 100 μM; lane 6, 120 μM; lane 7, 140 μM; lane 8, 160 μM; lane 9, 180 μM; lane 10, 200 μM; lane 11, 220 μM; lane 12, 240 μM.	296
Figure 6.24	Effect of various scavengers on the cleavage of pBR322 by 25 μM complex VOPhen . Lane 1, Gene Ruler 1 kb DNA ladder; Lane 2, DNA alone; Lane 3, DNA + 25 μM complex VOPhen + H ₂ O ₂ . Lanes 4 – 12 involves reaction of 25 μM complex VOPhen + H ₂ O ₂ with DNA in presence of various scavengers; lane 4, t-butyl alcohol (1 M); lane 5, 1 mM Mannitol; lane 6, DMSO (1 M); lane 7, 1 mM NaN ₃ ; lane 8, 10 mM NaN ₃ ; lane 9, 20 mM NaN ₃ ; lane 10, 30 mM NaN ₃ ; lane 11, 50 mM NaN ₃ ; lane 12, 100 mM NaN ₃ .	298
Figure 6.25	Effect of various scavengers on the cleavage of pBR322 by 120 μM complex VODMPhen . Lane 1, Gene Ruler 1 kb DNA ladder; Lane 2, DNA alone; Lane 3, DNA +120 μM complex VODMPhen + H ₂ O ₂ . Lanes 4 – 12 involves reaction of 120 μM complex VODMPhen + H ₂ O ₂ with DNA in presence of various scavengers; lane 4, t-butyl alcohol (1 M); lane 5, 1 mM Mannitol; lane 6, DMSO (1 M); lane 7, 1 mM NaN ₃ ; lane 8, 10 mM NaN ₃ ; lane 9, 20 mM NaN ₃ ; lane 10, 30 mM NaN ₃ ; lane 11, 50 mM NaN ₃ ; lane 12, 100 mM NaN ₃ .	298
Figure 6.26	Effect of various scavengers on the cleavage of pBR322 by 25 μM complex VODPPhen . Lane 1, Gene Ruler 1 kb DNA ladder; Lane 2, DNA alone; Lane 3, DNA + 25 μM complex VODPPhen + H ₂ O ₂ . Lanes 4 – 12 involves reaction of 25 μM complex VODPPhen + H ₂ O ₂ with DNA in presence of various scavengers; lane 4, t-butyl alcohol (1 M); lane 5, 1 mM Mannitol; lane 6, DMSO (1 M); lane 7, 1 mM NaN ₃ ; lane 8, 10 mM NaN ₃ ; lane 9, 20 mM NaN ₃ ; lane 10, 30 mM NaN ₃ ; lane 11, 50 mM NaN ₃ ; lane 12, 100 mM NaN ₃ .	299
Figure 6.27	Effect of various scavengers on the cleavage of pBR322 by 120 μM complex VODMPPhen . Lane 1, Gene Ruler 1 kb DNA ladder; Lane 2, DNA alone; Lane 3, DNA +120 μM complex VODMPPhen + H ₂ O ₂ . Lanes 4 – 12 involves reaction of 120 μM complex VODMPPhen + H ₂ O ₂ with DNA in presence of various scavengers; lane 4, t-butyl alcohol (1 M); lane 5, 1 mM Mannitol; lane 6, DMSO (1 M); lane 7, 1 mM NaN ₃ ; lane 8, 10 mM NaN ₃ ;	299

lane 9, 20 mM NaN₃; lane 10, 30 mM NaN₃; lane 11, 50 mM NaN₃; lane 12, 100 mM NaN₃.

LIST OF FIGURES

	Page
Appendix A UV-Vis spectrum of complex NaVO ₃ ($6.24 \times 10^{-5} \text{ mol L}^{-1}$; $\lambda = 264 \text{ nm}$, $\epsilon = 2402 \text{ mol}^{-1}\text{Lcm}^{-1}$; $\lambda = 205 \text{ nm}$, $\epsilon = 7491 \text{ mol}^{-1}\text{Lcm}^{-1}$)	323
Appendix B UV-Vis spectrum of complex VOSO ₄ ($4.73 \times 10^{-5} \text{ mol L}^{-1}$; $\lambda = 206 \text{ nm}$, $\epsilon = 3087 \text{ mol}^{-1}\text{Lcm}^{-1}$; $\lambda = 201 \text{ nm}$, $\epsilon = 2949 \text{ mol}^{-1}\text{Lcm}^{-1}$)	323
Appendix C UV-Vis spectrum of complex CuSO ₄ ($1.35 \times 10^{-4} \text{ mol L}^{-1}$; $\lambda = 237 \text{ nm}$, $\epsilon = 3431 \text{ mol}^{-1}\text{Lcm}^{-1}$)	324
Appendix D UV-Vis spectrum of complex CuCl ₂ ($8.92 \times 10^{-5} \text{ mol L}^{-1}$; $\lambda = 235 \text{ nm}$, $\epsilon = 3360 \text{ mol}^{-1}\text{Lcm}^{-1}$)	324

LIST OF TABLES

		Page
Table 1.1	Some of metal ions in clinical use	3
Table 1.2	The antibacterial and antiproliferative activities of some vanadium, copper and manganese complexes	5
Table 2.1	List of chemicals used in the synthesis	30
Table 2.2	List of complexes have been synthesized	37
Table 3.1	Crystal data, data collection and structure refinement parameters of complex VO₂PP	50
Table 3.2	Selected bond lengths (Å) and bond angles (°) of complex VO₂PP	52
Table 3.3	Hydrogen bonding distances and angles of complex VO₂PP	52
Table 3.4	Crystal data, data collection and structure refinement parameters of complex VO₂GLY	54
Table 3.5	Selected bond lengths (Å) and bond angles (°) of complex VO₂GLY	57
Table 3.6	Hydrogen bonding distances and angles of complex VO₂GLY	57
Table 3.7	Crystal data, data collection and structure refinement parameters of complex VOPYDC	59
Table 3.8	Selected bond lengths (Å) and bond angles (°) of complex VOPYDC	62
Table 3.9	Hydrogen bonding distances and angles of complex VOPYDC	62
Table 3.10	FT-IR analysis data of complexes VO₂PP , VO₂GLY and VO₂HPYDC	65
Table 3.11	FT-IR analysis data of complexes VOPYDC and VOMAL	71
Table 3.12	The UV-Vis analysis data of complexes VO₂PP , VO₂GLY , VO₂HPYDC , VOPYDC and VOMAL	76

LIST OF TABLES

		Page
Table 3.13	The ⁵¹ V-NMR chemical shift of complexes VO₂PP , VO₂GLY , VO₂HPYDC , VOPYDC and VOMAL	84
Table 3.14	The E _{pa} , E _{pc} , ΔE _p and E _{1/2} values of complexes VO₂PP , VO₂GLY , VOPYDC , VOMAL and VO₂HPYDC	90
Table 3.15	Concentration of complexes VO₂PP , VO₂GLY , VOPYDC , VOMAL and VO₂HPYDC that induce total cleavage of supercoil DNA	101
Table 3.16	Antibacterial activity of complexes VO₂PP , VO₂GLY , VOPYDC , VOMAL , VO₂HPYDC , VOSO ₄ and NaVO ₃ , results correspond to diameter of the inhibition zone(mm)	109
Table 3.17	Antibacterial activity of complexes VOPYDC , VO₂HPYDC and VOSO ₄ , the results are expressed as MIC (minimal inhibitory concentration)	110
Table 3.18	Antiproliferative activity of complexes VO₂PP , VO₂GLY , VOPYDC , VOMAL and VO₂HPYDC towards human cancer cell lines	112
Table 4.1	Crystal data, data collection and structure refinement parameters of complexes Cu-4-Cl-2-NO₂BZO and Cu-2-Cl-4-NO₂BZO	115
Table 4.2	Crystal data, data collection and structure refinement parameters of complexes Cu-2-Cl-6-FBZO and Cu-2-F-6-FBZO	116
Table 4.3	Crystal data, data collection and structure refinement parameters of complexes Cu-2-ClBZO and Cu-2-BrBZO	117
Table 4.4	Selected bond lengths (Å) and bond angles (°) of complex Cu-4-Cl-2-NO₂BZO	120
Table 4.5	Hydrogen bonding distances and angles of complex Cu-4-Cl-2-NO₂BZO	120
Table 4.6	Selected bond lengths (Å) and bond angles (°) of complex Cu-2-Cl-4-NO₂BZO	123

LIST OF TABLES

		Page
Table 4.7	Hydrogen bonding distances and angles of complex Cu-2-Cl-4-NO₂BZO	124
Table 4.8	Selected bond lengths (Å) and bond angles (°) of Cu-2-Cl-6-FBZO	126
Table 4.9	Hydrogen bonding distances and angles of Cu-2-Cl-6-FBZO	126
Table 4.10	Selected bond lengths (Å) and bond angles (°) of Cu-2-F-6-FBZO	129
Table 4.11	Hydrogen bonding distances and angles of Cu-2-F-6-FBZO	129
Table 4.12	Selected bond lengths (Å) and bond angles (°) of complex Cu-2-CIBZO	132
Table 4.13	Hydrogen bonding distances and angles of Cu-2-CIBZO	132
Table 4.14	Selected bond lengths (Å) and bond angles (°) of complex Cu-2-BrBZO	135
Table 4.15	Hydrogen bonding distances and angles of Cu-2-BrBZO	135
Table 4.16	Crystal data, data collection and structure refinement parameters of complex CuP-5-Cl-2-NO₂BZO	137
Table 4.17	Selected bond lengths (Å) and bond angles (°) of complex CuP-5-Cl-2-NO₂BZO	141
Table 4.18	Hydrogen bonding distances and angles of complex CuP-5-Cl-2-NO₂BZO	141
Table 4.19	FT-IR analysis data of complexes Cu-4-Cl-2-NO₂BZO , Cu-2-Cl-4-NO₂BZO , CuP-5-Cl-2-NO₂BZO , Cu-2-Cl-6-FBZO , Cu-2-F-6-FBZO , Cu-2-CIBZO and Cu-2-BrBZO	144
Table 4.20	The UV-Vis analysis data of complexes Cu-4-Cl-2-NO₂BZO , Cu-2-Cl-4-NO₂BZO , CuP-5-Cl-2-NO₂BZO , Cu-2-Cl-6-FBZO , Cu-2-F-6-FBZO , Cu-2-CIBZO and Cu-2-BrBZO	154

LIST OF TABLES

		Page
Table 4.21	The Epa, Epc, ΔE_p and $E_{1/2}$ values of complexes Cu-4-Cl-2-NO₂BZO , Cu-2-Cl-4-NO₂BZO , CuP-5-Cl-2-NO₂BZO , Cu-2-Cl-6-FBZO , Cu-2-F-6-FBZO , Cu-2-CIBZO and Cu-2-BrBZO	164
Table 4.22	Concentration of complexes Cu-4-Cl-2-NO₂BZO , Cu-2-Cl-4-NO₂BZO , CuP-5-Cl-2-NO₂BZO , Cu-2-Cl-6-FBZO , Cu-2-F-6-FBZO , Cu-2-CIBZO and Cu-2-BrBZO that induce total cleavage of supercoil DNA	177
Table 4.23	Antibacterial activity of complexes Cu-4-Cl-2-NO₂BZO , Cu-2-Cl-4-NO₂BZO , CuP-5-Cl-2-NO₂BZO and Cu-2-Cl-6-FBZO , results correspond to diameter of the inhibition zone (mm)	186
Table 4.24	Antibacterial activity of complexes Cu-2-F-6-FBZO , Cu-2-CIBZO and Cu-2-BrBZO , CuCl ₂ and CuSO ₄ , results correspond to diameter of the inhibition zone (mm)	187
Table 4.25	Antibacterial activity of complexes Cu-4-Cl-2-NO₂BZO , Cu-2-Cl-4-NO₂BZO , CuP-5-Cl-2-NO₂BZO , Cu-2-Cl-6-FBZO , Cu-2-F-6-FBZO , Cu-2-CIBZO and Cu-2-BrBZO against Gram negative bacteria <i>Enterobacter aerogenes</i> , the results are expressed as MIC (minimal inhibitory concentration)	188
Table 4.26	Antiproliferative activity of complexes Cu-4-Cl-2-NO₂BZO , Cu-2-Cl-4-NO₂BZO , CuP-5-Cl-2-NO₂BZO and Cu-2-Cl-6-FBZO towards human cancer cell lines	190
Table 4.27	Antiproliferative activity of complexes Cu-2-F-6-FBZO and Cu-2-CIBZO towards human cancer cell lines	191
Table 5.1	Crystal data, data collection and structure refinement parameters of complexes MnP-4-Cl-2-NO₂BZO and MnP-3-NO₂-5-NO₂BZO	194
Table 5.2	Crystal data, data collection and structure refinement parameters of complex Mn-4-NO₂BZO	195
Table 5.3	Selected bond lengths (Å) and bond angles (°) of complex MnP-4-Cl-2-NO₂BZO	197

LIST OF TABLES

		Page
Table 5.4	Hydrogen bonding distances and angles of complex MnP-4-Cl-2-NO₂BZO	197
Table 5.5	Selected bond lengths (Å) and bond angles (°) of complex MnP-3-NO₂-5-NO₂BZO	199
Table 5.6	Hydrogen bonding distances and angles of complex MnP-3-NO₂-5-NO₂BZO	200
Table 5.7	Selected bond lengths (Å) and bond angles (°) of complex Mn-4-NO₂BZO	202
Table 5.8	Hydrogen bonding distances and angles of complex Mn-4-NO₂BZO	202
Table 5.9	Crystal data, data collection and structure refinement parameters of complex MnP-4-NH₂BZO	204
Table 5.10	Selected bond lengths (Å) and bond angles (°) of complex MnP-4-NH₂BZO	207
Table 5.11	Hydrogen bonding distances and angles of complex MnP-4-NH₂BZO	207
Table 5.12	Crystal data, data collection and structure refinement parameters of complex MnP-4-FBZO	209
Table 5.13	Selected bond lengths (Å) and bond angles (°) of complex MnP-4-FBZO	212
Table 5.14	Hydrogen bonding distances and angles of complex MnP-4-FBZO	212
Table 5.15	Crystal data, data collection and structure refinement parameters of complex MnPGLY	214
Table 5.16	Selected bond lengths (Å) and bond angles (°) of complex MnPGLY	217
Table 5.17	Hydrogen bonding distances and angles of complex MnPGLY	217

LIST OF TABLES

		Page
Table 5.18	The FT-IR analysis data of complexes MnP-4-Cl-2-NO₂BZO , MnP-3-NO₂-5-NO₂BZO , Mn-4-NO₂BZO , MnP-4-NH₂BZO , MnP-4-FBZO , MnP-4-CIBZO , MnPGLY and MnPyr	222
Table 5.19	The UV-Vis analysis data of complexes MnP-4-Cl-2-NO₂BZO , MnP-3-NO₂-5-NO₂BZO , Mn-4-NO₂BZO , MnP-4-NH₂BZO , MnP-4-FBZO , MnP-4-CIBZO , MnPGLY and MnPyr	233
Table 5.20	The Epa, Epc, ΔEp and E _{1/2} values of complexes MnP-4-Cl-2-NO₂BZO , MnP-3-NO₂-5-NO₂BZO , Mn-4-NO₂BZO , MnP-4-NH₂BZO , MnP-4-FBZO , MnP-4-CIBZO , MnPGLY and MnPyr	244
Table 5.21	Concentration of complexes MnP-4-Cl-2-NO₂BZO , MnP-3-NO₂-5-NO₂BZO , Mn-4-NO₂BZO , MnP-4-NH₂BZO , MnP-4-FBZO , MnP-4-CIBZO , MnPGLY and MnPyr that induce total cleavage of supercoil DNA	259
Table 5.22	Antibacterial activity of complexes MnP-4-Cl-2-NO₂BZO , MnP-3-NO₂-5-NO₂BZO , Mn-4-NO₂BZO , MnP-4-NH₂BZO , results correspond to diameter of the inhibition zone (mm)	266
Table 5.23	Antibacterial activity of complexes MnP-4-FBZO , MnP-4-CIBZO , MnPGLY , MnPyr and MnCl ₂ , results correspond to diameter of the inhibition zone (mm)	267
Table 5.24	Antiproliferative activity of complexes MnP-4-Cl-2-NO₂BZO , MnP-3-NO₂-5-NO₂BZO , Mn-4-NO₂BZO , MnP-4-NH₂BZO and MnPyr towards human cancer cell lines	269
Table 6.1	FT-IR analysis data of complexes VOPhen , VODMPhen , VODPPhen and VODMPPhen	273
Table 6.2	The UV absorption data of complexes VOPhen , VODMPhen , VODPPhen and VODMPPhen upon addition of increasing concentration of CT-DNA	285
Table 6.3	Antibacterial activity of complexes VOPhen , VODMPhen , VODPPhen and VODMPPhen , results correspond to diameter of the inhibition zone (mm)	302

LIST OF TABLES

	Page
Table 6.4 Antibacterial activity of complexes VOPhen , VODMPhen , VODPPhen and VODMPPhen , the results are expressed as MIC (minimal inhibitory concentration)	303

LIST OF ABBREVIATIONS AND SYMBOLS

Cu-2-F-6-FBZO	tetrakis(μ -2,6-difluorobenzoato- $\kappa^2 O, O'$)bis[aquacopper(II)]
Cu-2-BrBZO	tetrakis(μ -2-bromobenzoato- $\kappa^2 O, O'$)bis[aquacopper(II)]
Cu-2-Cl-4-NO₂BZO	tetrakis(μ -2-chloro-4-nitrobenzoato- $\kappa^2 O, O'$)bis[aquacopper(II)]
Cu-2-Cl-6-FBZO	tetrakis(μ -2-chloro-6-fluorobenzoato- $\kappa^2 O, O'$)bis[aquacopper(II)]
Cu-2-ClBZO	tetrakis(μ -2-chloro-benzoato- $\kappa^2 O, O'$)bis[aquacopper(II)]
Cu-4-Cl-2-NO₂BZO	tetrakis(μ -4-chloro-2-nitrobenzoato- $\kappa^2 O, O'$)bis[aquacopper(II)]
CuP-5-Cl-2-NO₂BZO	catena-poly[[bis(5-chloro-2-nitrobenzoato)copper(II)]bis(μ -5-chloro-2-nitrobenzoato)]
Hela	Human cervical cancer cell line
HepG2	Human liver cancer cell line
IC₅₀	A measure of the concentration of particular drug that inhibit the biological process of cells by half
bp	base pair
LC₅₀	A measure of the concentration of particular drug that kill 50 % of the cells
LMCT	Ligand to Metal Charge Transfer
MCF-7	Human breast cancer cell line
MDA-MB-231	Human invasive breast cancer cell line
MIC	minimal inhibitory concentration
Mn-4-NO₂BZO	tetraaquabis(4-nitrobenzoato)manganese(II) hydrate

LIST OF ABBREVIATIONS AND SYMBOLS

MnP-4-CIBZO	catena-poly[[diaquabis(4-chlorobenzoato)manganese(II)]bis(μ -4-chlorobenzoato)]
MnP-4-Cl-2-NO₂BZO	catena-poly[[diaquabis(4-chloro-2-nitrobenzoato)manganese(II)]bis(μ -4-chloro-2-nitrobenzoato)]
MnP-4-FBZO	catena-poly[[diaquabis(4-flourobenzoato)manganese(II)]bis(μ -4-flourobenzoato)]
MnP-4-NH₂BZO	catena-poly[[bis(4-aminobenzoato)manganese(II)]tri(μ -4-aminobenzoato)]
MnPGLY	catena-poly[[aqua(diglycolato)manganese(II) hydrate)]bis(μ -diglycolato)]
MnPyr	diaquabis(pyridine-2-carboxylato)manganese(II) hydrate
MTT	(3-[4,5-dimethylthiazol-2-yl]-2,5-diphenyltetrazolium bromide)
NMR	Nuclear Magnetic Resonance
ROS	Reactive oxygen species
SRB	Sulforhodamine B
TGI	Cytostatic activity = A measure of the concentration of particular drug that inhibit total growth of cell lines.
UV-Vis	Ultraviolet-Visible
VO₂GLY	sodium (diglycolato)dioxovanadium(V) dihydrate
VO₂HPYDC	Sodium (4-hydroxypyridine-2,6-dicarboxylato)dioxovanadium(V) dihydrate
VO₂PP	(pyridine-2-carboxylato)(pyridinium-2-carboxylato)dioxovanadium(V) monohydrate

LIST OF ABBREVIATIONS AND SYMBOLS

VODMPhen	aqua(2,9-dimethyl-1,10-phenanthroline) sulfatooxovanadium(IV)
VODMPPhen	aqua(2,9-dimethyl-4,7-diphenyl-1,10-phenanthroline) sulfatooxovanadium(IV) hydrate
VODPPhen	aqua(4,7-diphenyl-1,10-phenanthroline) sulfatooxovanadium(IV) hydrate
VOMAL	disodium diaquabis(malonato)oxovanadium(IV)
VOPhen	aqua(1,10-phenanthroline)sulfatooxovanadium(IV)
VOPYDC	diaqua(pyridine-2,6-carboxylato)oxovanadium(IV)ethanol solvate
ΔE_p	$E_{pa} - E_{pc}$
V^V	Vanadium V
V^{IV}	Vanadium IV
ϵ	Molar absorptivity

**SINTESIS, PENCIRIAN, SIFAT-SIFAT NUCLEOLITIK,
ANTIBAKTERIA DAN
ANTIPOLIFERATIF BAGI KOMPLEKS VANADIUM, KUPRUM
DAN MANGAN**

ABSTRAK

Siri kompleks bagi vanadium karboksilato, kuprum karboksilato, mangan karboksilato dan terbitan vanadium fenantrolina telah disintesis dan dicirikan. Maklumat penuh tentang kompleks ditunjukkan dalam Jadual 2.2 (muka surat 37). Kompleks ini telah dicirikan dengan menggunakan kristalografi X-ray, analisis unsur, FT-IR, spektroskopi UV-Vis dan siklik voltammetrik. Dalam kajian elektrokimia, kompleks vanadium karboksilato telah menunjukkan aktif redok dengan mempamerkan pasangan redok kuasi-berbalik yang selaras dengan V^V/V^{IV} proses redok, manakala kompleks kuprum karboksilato telah menunjukkan aktif redok dengan mempamerkan dua pasangan redok kuasi-berbalik yang selaras dengan $Cu^{II}Cu^{II}/Cu^{II}Cu^I$ dan $Cu^{II}Cu^I/Cu^ICu^I$ proses redok dan mangan karboksilato telah menunjukkan aktif redok dengan mempamerkan pasangan redok kuasi-berbalik yang selaras dengan Mn^{II}/Mn^{III} proses redok. Dalam kajian nukleolitik, semua kompleks didapati boleh mengakibatkan pengoksidaan belahan DNA tetapi dengan cara yang berbeza. Kompleks kuprum karboksilato dan mangan karboksilato boleh mengakibatkan belahan DNA dalam kehadiran H_2O_2 . Sementara itu,

untuk kompleks vanadium karboksilato, kompleks vanadium(V) karboksilato memerlukan H_2O_2 untuk mengakibatkan belahan DNA manakala kompleks vanadium(IV) karboksilato tidak memerlukan H_2O_2 untuk mengakibatkan belahan DNA. Bagi kompleks terbitan vanadium fenantrolina pula, mereka boleh mengakibatkan belahan DNA dalam kehadiran H_2O_2 dan dalam keadaan tanpa H_2O_2 . Walaubagaimanapun, aktiviti belahan DNA meningkat secara mendadak dalam kehadiran H_2O_2 . Agen perencet reaktif spesies oksigen (ROS) juga telah digunakan untuk menentukan spesies reaktif yang bertanggungjawab dalam belahan DNA. Hidroksil radikal dan oksigen tunggal adalah ROS yang bertanggungjawab dalam belahan DNA. Dalam penyaringan antibakteria, semua kompleks kecuali kompleks mangan karboksilato mempamerkan aktiviti antibakteria terhadap spesies bakteria Gram positif atau Gram negatif. Kompleks kuprum karboksilato menunjukkan aktiviti antibakteria yang sangat selektif di mana mereka hanya menunjukkan aktiviti antibakteria terhadap *Enterobacter aerogenes* berGram negatif bakteria. Aktiviti antibakteria kompleks terbitan vanadium fenantrolina telah menunjukkan bahawa kumpulan metil yang terikat pada kedudukan 2 dan 9 pada gelang fenantrolina dapat meningkatkan aktiviti antibakteria. Dalam penyaringan antiproliferatif, secara umum kompleks vanadium karboksilato mempamerkan aktiviti antiproliferatif yang lebih tinggi berbanding dengan kompleks kuprum karboksilato dan mangan karboksilato. Kompleks kuprum karboksilato dan mangan karboksilato menunjukkan selektiviti sitotoksik terhadap garisan sel kanser HepG2 apabila dibandingkan dengan garisan sel kanser MCF-7 dan Hela. Eksperimen nukleolitik telah menyarankan bahawa belahan atau fragmentasi DNA oleh ROS yang dihasilkan oleh kompleks berkemungkinan besar bertanggungjawab terhadap aktiviti antiproliferatif yang dipamerkan oleh kompleks.

**Synthesis, Characterization, Nucleolytic, Antibacterial and
Antiproliferative Properties of Vanadium, Copper and Manganese
Complexes**

ABSTRACT

Series of vanadium carboxylato complexes, copper carboxylato complexes, manganese carboxylato complexes and vanadium phenanthroline derivative complexes have been synthesized and characterized. The details of all the complexes are tabulated in Table 2.2 (page 37). The complexes have been characterized by X-ray crystallography, elemental analysis, FT-IR, UV-Vis spectroscopy and cyclic voltammetry. In electrochemistry studies, vanadium carboxylato complexes show redox active by displaying a quasi-reversible redox couple corresponding to V^V/V^{IV} redox process while copper carboxylato complexes show redox active by displaying two quasi-reversible redox couples corresponding to $Cu^{II}Cu^{II}/Cu^{II}Cu^I$ and $Cu^{II}Cu^I/Cu^ICu^I$ redox processes and manganese carboxylato complexes show redox active by displaying a quasi-reversible redox couple corresponding to Mn^{II}/Mn^{III} redox process. In nucleolytic studies, all the complexes can induce oxidative DNA cleavage but in different manner. The copper carboxylato complexes and manganese carboxylato complexes can induce DNA cleavage in the presence of H_2O_2 . Meanwhile for vanadium carboxylato complexes, vanadium(V) carboxylato complexes require H_2O_2 to induce DNA cleavage while vanadium(IV) carboxylato complexes do not require H_2O_2 to induce DNA cleavage. As

for vanadium phenanthroline derivative complexes, they can induce DNA cleavage in the presence and in the absence of H_2O_2 . However, the DNA cleavage activity of the vanadium phenanthroline derivative complexes is greatly enhanced in the presence of H_2O_2 . Reactive oxygen species (ROS) scavengers have also been used to ascertain the reactive species responsible for DNA cleavage. The hydroxyl radical and singlet oxygen species have been found to be the ROS that are responsible in the DNA cleavage reaction. In the antibacterial screening, all the complexes except manganese carboxylato complexes exhibit antibacterial activity against certain Gram negative or Gram positive bacteria species. Copper carboxylato complexes show a very selective antibacterial activity whereby they only exhibit antibacterial activity against Gram negative bacteria *Enterobacter aerogenes*. The antibacterial activity of vanadium phenanthroline derivative complexes reveals that methyl groups attached at the position 2 and 9 in phenanthroline ring may increase the complexes antibacterial activity. In antiproliferative screening, vanadium carboxylato complexes in general exhibit higher antiproliferative activity when compared to copper carboxylato complexes and manganese carboxylato complexes. Copper carboxylato complexes and manganese carboxylato complexes exhibit cytotoxic selectivity against HepG2 cancer cell line when compared to MCF-7 and Hela cancer cell lines. The nucleolytic experiments suggest that the cleavage or fragmentation of DNA by ROS generated by the complexes maybe responsible for the antiproliferative activity exhibited by the complexes.

Keywords: Vanadium Complexes; Copper Complexes; Manganese Complexes; DNA Cleavage; Antibacterial; Antiproliferative

CHAPTER 1

INTRODUCTION

1.1 Biological roles and medicinal applications of metal complexes and metal ions

Studies on biological activities of metal complexes have been one of our long-term interests. Metal complexes are well known to exhibit antibacterial, antiproliferative, antiapoptotic, anti-inflammatory and insulin mimetic properties [1-28]. Several of the metal complexes have entered clinical trials and few have been registered for clinical use [29-31]. Platinum based complexes such as cisplatin, carboplatin and oxaliplatin are widely used as chemotherapeutic agents against ovarian, lung, head, neck and colorectal cancers, and have greatly improving the survival rates of patients worldwide. Schematic structures of cisplatin, carboplatin and oxaliplatin are depicted in Figure 1.1. These platinum complexes react *in vivo*, crosslink the DNA in several different ways and subsequently interfering the cell division by mitosis. The damaged DNA elicits DNA repair mechanisms, which in turn activate apoptosis when repair proves impossible. Meanwhile, Aurum(I) thiolate drugs such as aurothiomalate (Myocrisin^R), aurothioglucose (Solganol^R), aurothiopropionol sulfonate (Allochrysin^R), and the oral drug auranofin (Ridaura^R), are widely used for the treatment of difficult cases of rheumatoid arthritis. Bismuth(III) compounds such as bismuth subcitrate and subsalicylate are widely used for the treatment of diarrhoea, dyspepsia and gastric and duodenal ulcers. Bismuth(III) compounds are found to be antibacterial active against

bacteria *Helicobacter pylori* which is associated with the mucus layer of ulcers. Sodium nitroprusside ($\text{Na}_2[\text{Fe}^{\text{II}}(\text{CN})_5(\text{NO})] \cdot 2\text{H}_2\text{O}$ or (Nipride^R) is used to treat hypotensive while Cu-salicylate (Alcusal^R) is used to treat inflammatory. The success of metal complexes in medicinal applications has aroused great interest in the development of new metal complexes to diagnose and treat diseases including cancers, bacteria and virus infection related diseases, inflammatory and diabetes.

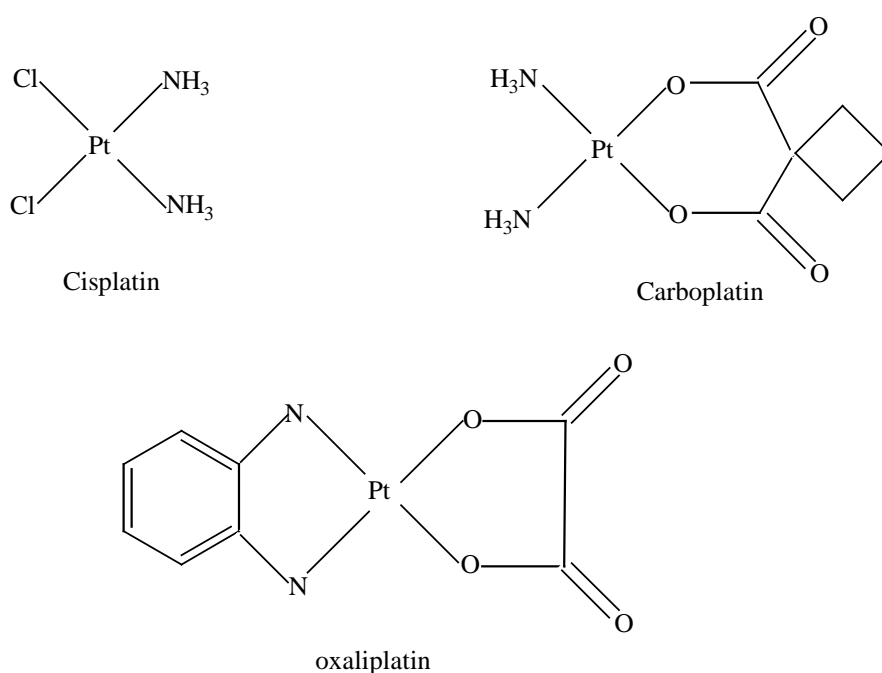


Figure 1.1: Schematic structures of cisplatin, carboplatin and oxaliplatin

Apart from metal complexes, metal ion or inorganic elements play essential roles in biological and biomedical processes in human health and disease as metalloenzymes and metalloproteins [29]. As metalloproteins, metal ions perform as catalyst or stabilizer to stabilize the protein tertiary or quaternary structure. In addition, many proteins need to bind one or more metal ions to perform their functions. Complex zinc ion is one of the

most important components of metalloproteins in the human body, which functions as DNA transcription and regulation as well as oxidation and hydrolysis, cleavage of peptide bonds as well as formation of phosphodiester bonds. Meanwhile, copper ion is presence in some of the most important metalloenzymes in the human body and functions as superoxide dismutase to neutralize free radical generated from various human biological systems. Metal ions are also very important for the structure and function (in the case of RNA) of nucleic acids. Besides, many organic compounds used in medicine do not have a purely organic mode of action; some are activated or biotransformed by metal ions including metalloenzymes, others have a direct or indirect effect on metal ion metabolism. Some of the metal ions have also been registered for clinical used as therapy and diagnosis agents, as listed in Table 1.1.

Table 1.1: Some of metal ions in clinical use

Compounds	Function/Treat
Li_2CO_3	Prophylaxis for bipolar disorders
CaCO_3 , $\text{Mg}(\text{OH})_2$	Antacid
$\text{La}_2^{\text{III}}(\text{CO}_3)_3$	Chronic renal failure
MgSO_4	Hypomagnesemia
Potassium citrate	Kidney stones
Magnesium citrate	Saline laxative

1.2 Antibacterial and antiproliferative activities of transition metal complexes

Transition metal complexes such as vanadium, copper and manganese complexes are known to exhibit excellent antibacterial and antiproliferative activities. The summary of antibacterial and antiproliferative activities of selected few vanadium, copper and manganese complexes that have already described in the literatures is tabulated in Table 1.2. Referring to Table 1.2, it can be seen that transition metal complexes are rich in antibacterial and antiproliferative activities, being active against a wide spectrum of bacteria species or cancer cells. Transition metal complexes may induce cell death through disruption of the cell cycle or by DNA strand scission [32]. There are evidences to indicate that metal complexes can induce DNA strand scission not directly reacting with DNA components but acting mainly through the production of highly reactive oxygen species, especially hydroxyl radicals generated in cells. These reactive oxygen species actually cause the DNA strand scission. Transition metal complexes through Fenton-like reactions and/or during the intracellular reduction can generate reactive oxygen species. Besides, some transition metal complexes, which are photoactivatable, can induce DNA cleavage upon UV irradiation and singlet oxygen is the common reactive oxygen species that is generated in this process. Rich diversity of antibacterial and antiproliferative activities by transition metal complexes provides exciting prospects for the design of novel therapeutic agents with unique mechanisms of action to act against certain bacteria or cancers, as different metal complexes can produce different therapeutic effect. Therefore, detailed investigations could be helpful in designing more potent antibacterial and anticancer agents for the therapeutic use.

Table 1.2: The antibacterial and antiproliferative activities of some vanadium, copper and manganese complexes

Complexes	Antibacterial/ Antiproliferative activity	Bacteria species/Cancer cells	Ref:
$[\text{Cu}^{\text{II}}(4-(2\text{-pyridylmethyl})-1,7\text{-dimethyl-1,4,7-triazonane-2,6-dione})(\text{CH}_3\text{CN})_2](\text{ClO}_4)_2$	Antibacterial	Escherichia coli (T7), Staphylococcus aureus, Pseudomonas aeruginosa	13
$\text{Cu}^{\text{II}}(2\text{-furancarbaldehyde thiosemicarbazone}) 0.5\text{H}_2\text{O}$	Antibacterial	Bacillus subtilis, Staphylococcus aureus	18
$[\text{Cu}_2^{\text{II}}(\text{N,N}'\text{-bis}(3\text{-aminopropyl})\text{oxamide})(2,2'\text{-bipyridine})(2,4,6\text{-trinitrophenol})(\text{H}_2\text{O})](2,4,6\text{-trinitrophenol})$	Antibacterial	Escherichia coli, Bacillus subtilis, Staphylococcus aureus	16
$\text{Cu}^{\text{II}}_2(\text{N,N}'\text{-bis}(\text{N-hydroxyethylaminoethyl})\text{oxamide})(2,4,6\text{-trinitrophenol})_2$	Antiproliferative	SMMC-7721 human hepatocellular carcinoma cells, A549 human lung adenocarcinoma cells	8
$\text{Cu}^{\text{II}}(\text{ethyl } 2\text{-bis}(2\text{-pyridylmethyl})\text{aminopropionate})\text{Cl}_2$	Antiproliferative	Eca-109 human esophageal cancer cells, A549 human lung adenocarcinoma cells	10
$\text{Cu}^{\text{II}}(\text{norfloxacinato})(2,2'\text{-bipyridine})\text{Cl}_2$	Antiproliferative	HL-60 and K562 human leukemia cells	19

Table 1.2: Continued

Complexes	Antibacterial/ Antiproliferative activity	Bacteria species/Cancer cells	Ref:
Mn ^{II} (tetraphenyl porphyrin), (ebselen–porphyrin conjugate)	Antibacterial	Staphylococcus aureus	15
Mn ^{II} (tetraamide macrocyclic)NO ₃	Antibacterial	Pseudomonas cepacicola, Klebsella aerogenous	25
Mn ^{II} (6,7-dicyanodipyrido[2,2- <i>d</i> :29,39- <i>f</i>]quinoxaline) (NO ₃)(H ₂ O)]NO ₃ .CH ₃ OH	Antiproliferative	BGC-823 human stomach cancer cells, HL-60 human leukemia cells	27
V ^V ₄ O ₁₀ (μ-O) ₂ [VO(H- ciprofloxacin) ₂] ₂ .13H ₂ O	Antibacterial	Staphylococcus aureus, Escherichia coli, Pseudomonas aeruginosa	21
V ^V (2-methyl-3H-5-hydroxy-6- carboxy-4-pyrimidinone ethyl ester)	Antiproliferative	Hela human cervical cancer cells	6
V ^V O ₂ (salicylaldehydesemicarbazone)	Antiproliferative	MC3T3-E1 osteoblastic mouse calvaria-derived cells, UMR106 rat osteosarcoma- derived cells	12
V ^{IV} O(3-amino-6(7)- chloroquinoxaline-2-carbonitrile N ¹ , N ⁴ -dioxide) ₂	Antiproliferative	V79 chinese hamster lung fibroblasts cells	24

1.3 Background of nucleolytic activity of metal complexes

Recently, research on nucleolytic activity of metal complexes has blossomed leading to the discovery of the capacity of metal complexes to interact with DNA and further to induce DNA cleavage in the presence of co-factor. Transition metal complexes such as ruthenium, copper, cobalt, manganese and vanadium complexes have been reported to promote DNA cleavage in the presence of co-factor [33-55]. The DNA cleavage by metal complexes can occur via oxidative, photolytic and hydrolytic cleavage.

Double helical DNA consists of two complementary, antiparallel polydeoxyribonucleotide strands associated by specific hydrogen bonding interactions between nucleotide bases, Figure 1.2. The backbone of the DNA strand is made from alternating phosphate and sugar residues. The sugar in DNA is 2-deoxyribose, which is a pentose (five-carbon) sugar. The sugars are joined together by phosphate groups that form phosphodiester bonds between the third and fifth carbon atoms of adjacent sugar rings. The sugar phosphate backbone of paired strands defines the helical grooves, within which the edges of the heterocyclic bases are exposed. The biologically relevant B-form structure of the DNA double helix is characterized by a shallow, wide major groove and a deep, narrow minor groove. The major and minor grooves provide a lot of hydrogen binding sites. The DNA double helix is stabilized by hydrogen bonds between the nucleotide bases attached to the two strands. The four bases found in DNA are adenine, cytosine, guanine and thymine, Figure 1.3. These four bases are attached to the sugar/phosphate to form the complete nucleotide.

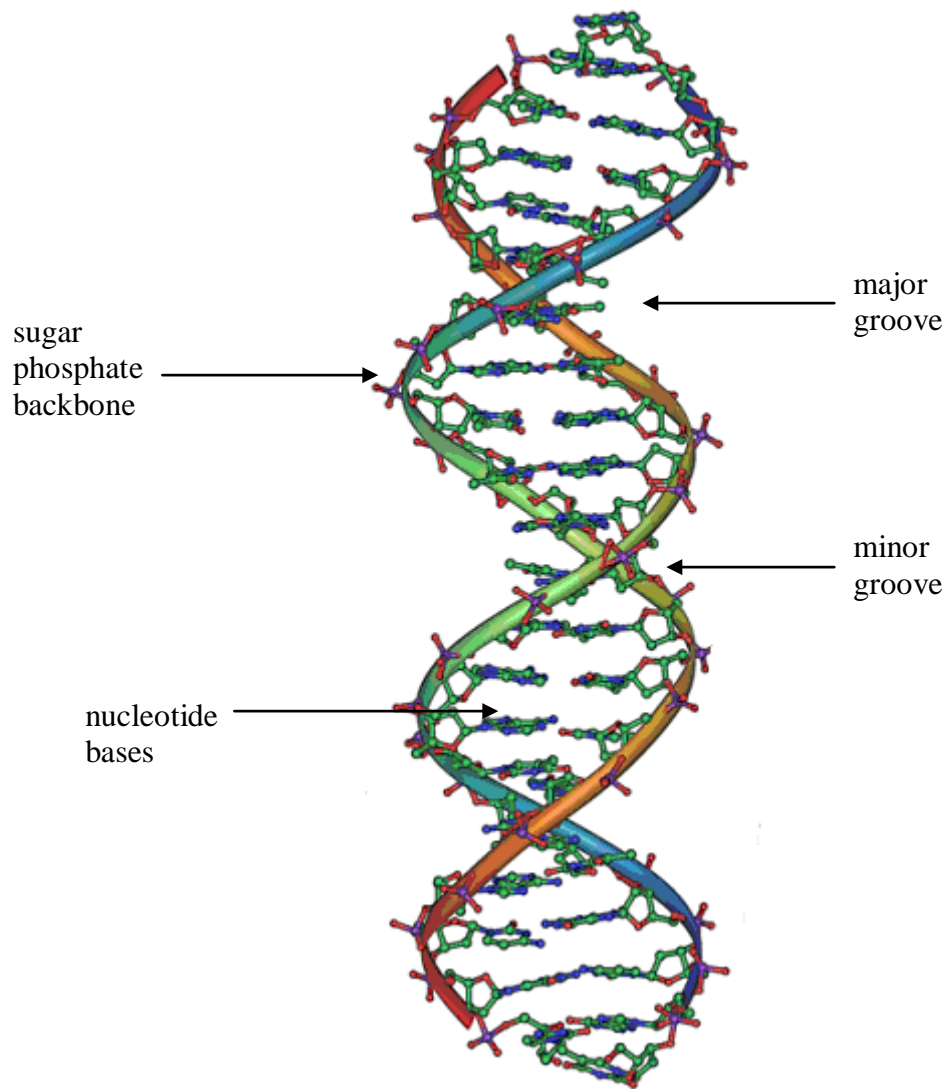


Figure 1.2: The structure of part of a DNA double helix

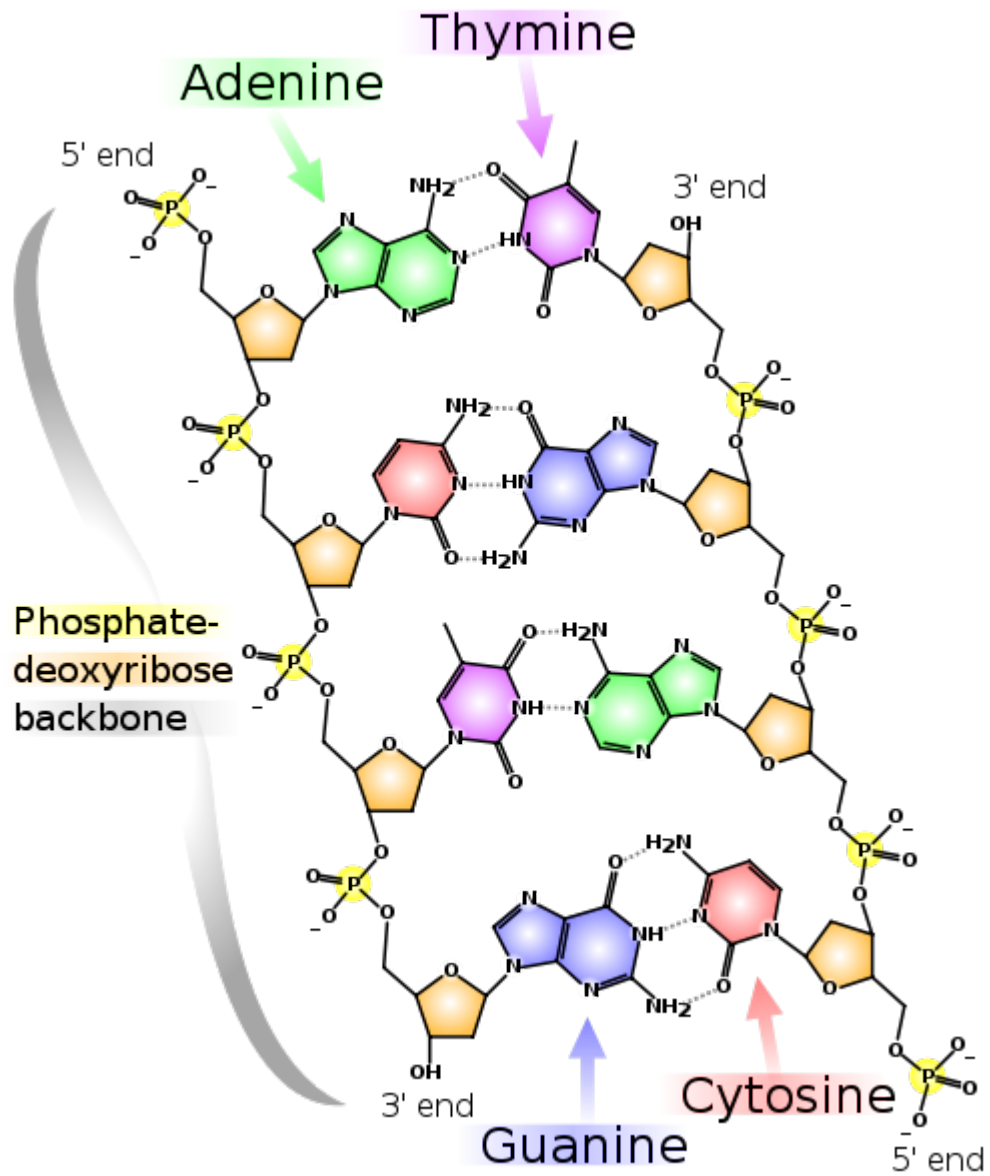


Figure 1.3: The chemical structure of DNA. Hydrogen bonds are shown as dotted lines

The DNA cleavage by metal complexes can be monitored by agarose gel electrophoresis. The DNA strain that was used in DNA cleavage studies is pBR322 DNA. The pBR322 DNA is a double helix DNA and it exists in supercoil form. In general, if scission or cleavage occurs on one strand of the supercoil DNA, the supercoil (Form I) will relax and convert to nicked form (Form II) while if scission occurs on both strands, a linear form (Form III) will be generated (Figure 1.4). These three forms of DNA will migrate in different rate in gel electrophoresis (Figure 1.5) with supercoil form migrates the fastest while nicked form migrates the slowest and linear form migrates in between supercoil and nicked forms. DNA cleavage by metal complexes is varied among the complexes, with some metal complexes can induce both single and double strand scissions while some metal complexes can only induce single scission.

In oxidative and photolytic DNA cleavage, metal complexes cannot induce DNA cleavage directly but indirectly through generating reactive oxygen species (ROS) such as hydroxyl radical and singlet oxygen. These ROS are actually responsible in DNA cleavage reaction. In order to study the DNA cleavage mechanism by metal complexes, various inhibiting agents have been used such as DMSO, t-butanol, mannitol and sodium azide. DMSO, t-butanol and mannitol are used as hydroxyl radical inhibitors while sodium azide is used as singlet oxygen inhibitor. Meanwhile in hydrolytic DNA cleavage, metal complexes can induce DNA cleavage directly by cleaving the P-O bonds in the phosphodiester of DNA.

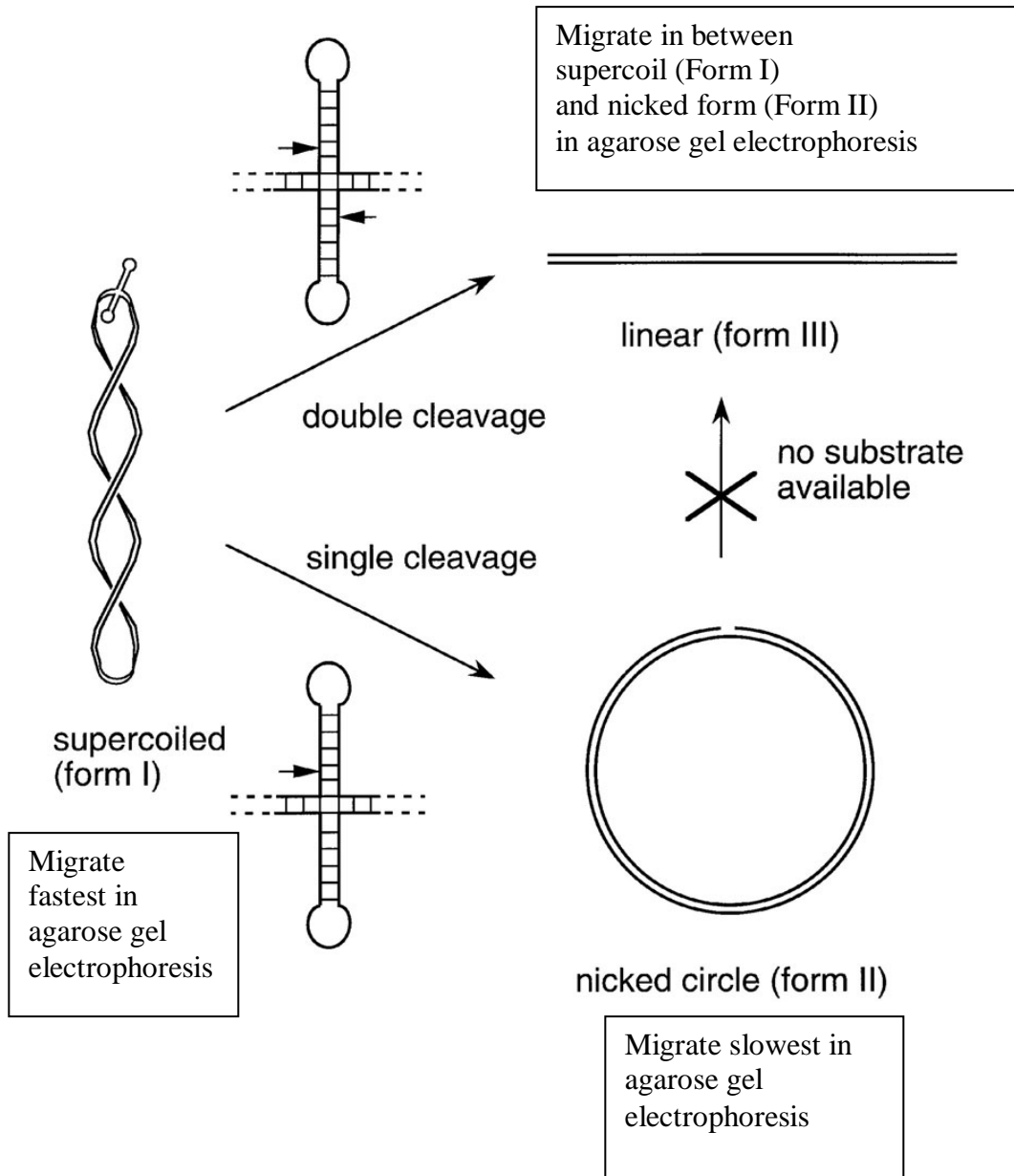


Figure 1.4: Supercoiled, nicked and linear DNA

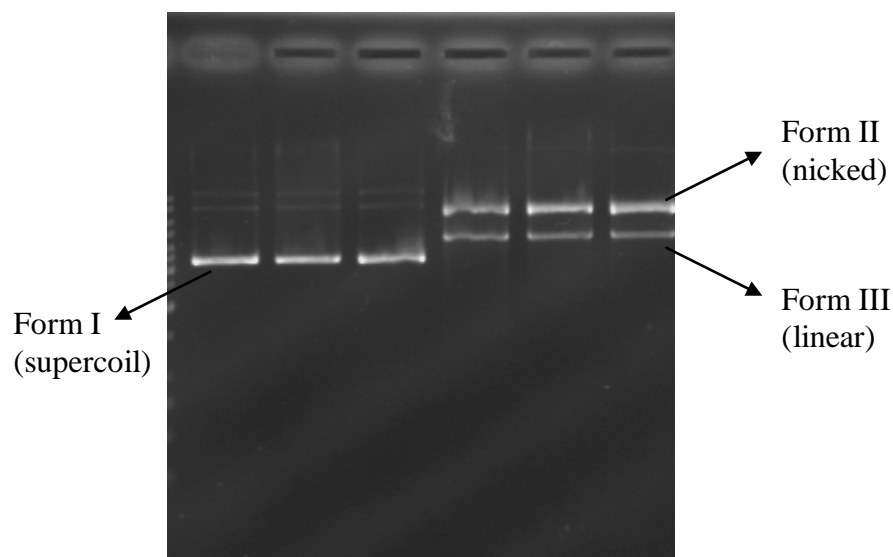


Figure 1.5: Supercoiled, nicked and linear DNA bands in gel electrophoresis diagram

1.3.1 Oxidative DNA cleavage by metal complexes in the presence of 3-mercaptopropionic acid (MPA)

Complexes $[\text{Cu}^{\text{II}}(\text{ternary-L-glutamine})(1,10\text{-phenanthroline})(\text{H}_2\text{O})](\text{ClO}_4)$ and $[\text{Cu}^{\text{II}}(\text{ternary-S-methyl-L-cysteine})(1,10\text{-phenanthroline})(\text{H}_2\text{O})](\text{ClO}_4)$ (Figure 1.6) can exhibit oxidative DNA cleavage in the presence of 3-mercaptopropionic acid (MPA) [33, 34]. MPA plays as reduction agent in the DNA cleavage reaction. Both of the complexes can only induce single DNA scission by converting supercoil DNA to nicked form. The mechanistic aspects of the DNA cleavage reactions have been investigated with various inhibiting agents and the results show that hydroxyl radical scavenger DMSO can inhibit the DNA cleavage induced by both of the complexes. This indicates the involvement of

hydroxyl radical in the cleavage reaction. The proposed DNA cleavage mechanism of metal complex in the presence of MPA is illustrated in Figure 1.7.

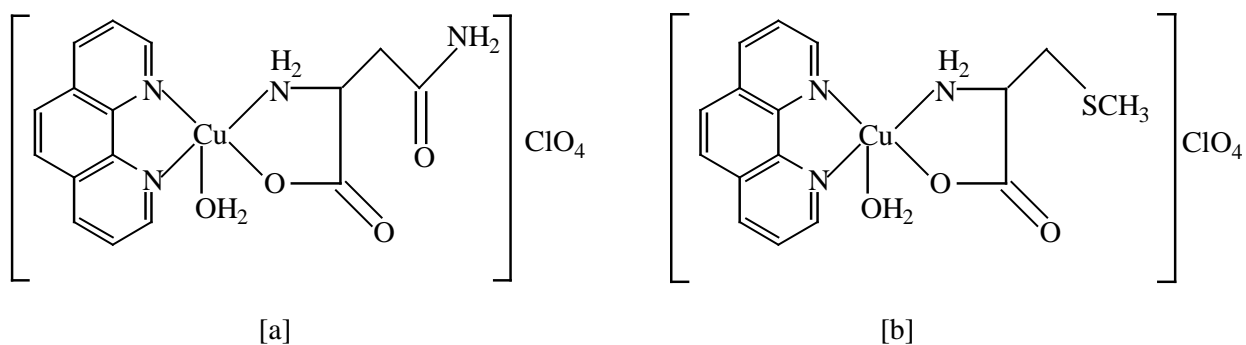


Figure 1.6: The schematic structures;

- a) $[\text{Cu}^{\text{II}}(\text{ternary-L-glutamine})(1,10\text{-phenanthroline})(\text{H}_2\text{O})](\text{ClO}_4)$
 b) $[\text{Cu}^{\text{II}}(\text{ternary-S-methyl-L-cysteine})(1,10\text{-phenanthroline})(\text{H}_2\text{O})](\text{ClO}_4)$

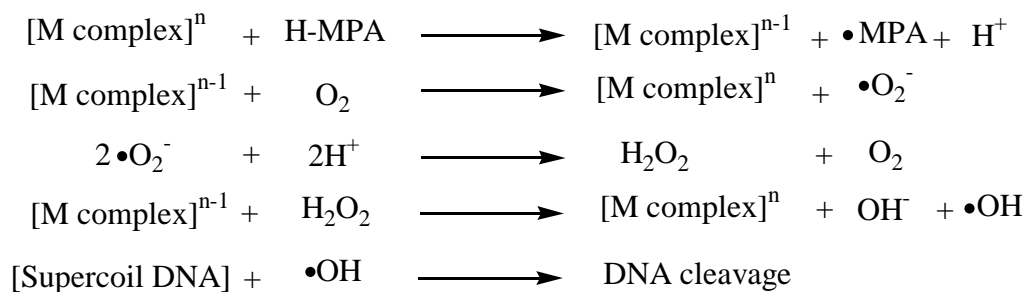


Figure 1.7: The proposed DNA cleavage mechanism of metal complex in the presence of 3-mercaptopropionic acid (MPA)

1.3.2 Oxidative DNA cleavage by metal complexes in the presence of ascorbic acid

Complexes $[\text{Ru}^{\text{II}}(\text{imidazo}[4,5-f][1,10]\text{phenanthroline})(\text{NH}_3)_4](\text{PF}_6)_2$ and $[\text{Cu}^{\text{II}}(\text{L-threonine})(1,10\text{-phenanthroline})(\text{H}_2\text{O})](\text{ClO}_4)$ (Figure 1.8) can induce oxidative DNA cleavage in the presence of ascorbic acid [35, 36]. Similar to MPA, ascorbic acid also acts as the reduction agent in the DNA cleavage reaction. Complex $[\text{Ru}^{\text{II}}(\text{imidazo}[4,5-f][1,10]\text{phenanthroline})(\text{NH}_3)_4](\text{PF}_6)_2$ can only induce single DNA scission by converting supercoil DNA to nicked form while complex $[\text{Cu}^{\text{II}}(\text{L-threonine})(1,10\text{-phenanthroline})(\text{H}_2\text{O})](\text{ClO}_4)$ can induce both single and double DNA scissions by converting supercoil DNA to nicked and linear forms. In comparison, complex $[\text{Cu}^{\text{II}}(\text{L-threonine})(1,10\text{-phenanthroline})(\text{H}_2\text{O})](\text{ClO}_4)$ appears to be a better DNA cleaver when compared to complex $[\text{Ru}^{\text{II}}(\text{imidazo}[4,5-f][1,10]\text{phenanthroline})(\text{NH}_3)_4](\text{PF}_6)_2$ in the presence of ascorbic acid. In mechanistic studies, it is evident that the hydroxyl radical scavenger DMSO diminish significantly the nuclease activity of complex $[\text{Cu}^{\text{II}}(\text{L-threonine})(1,10\text{-phenanthroline})(\text{H}_2\text{O})](\text{ClO}_4)$, which is indicative of the involvement of the hydroxyl radical in the cleavage process. The proposed DNA cleavage mechanism of metal complex in the presence of ascorbic acid is illustrated in Figure 1.9.

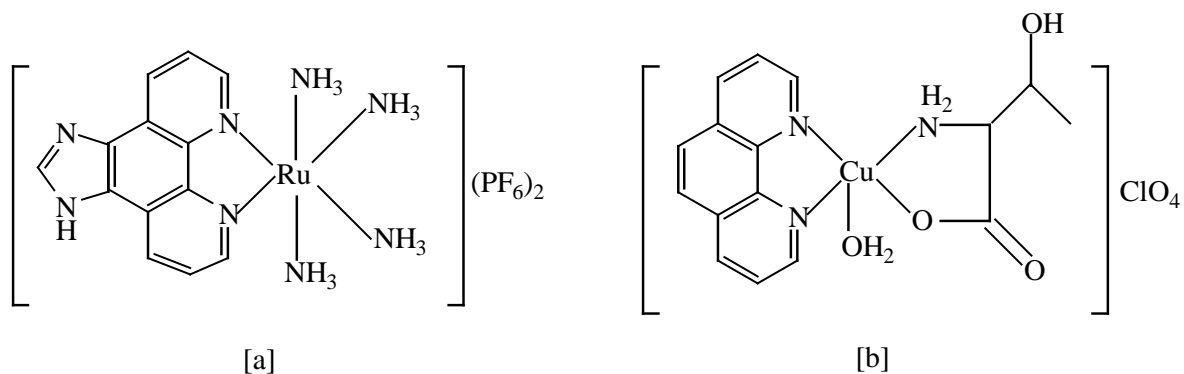


Figure 1.8: The schematic structures;
 a) $[\text{Ru}^{\text{II}}(\text{imidazo}[4,5\text{-}f][1,10]\text{phenanthroline})(\text{NH}_3)_4](\text{PF}_6)_2$
 b) $[\text{Cu}^{\text{II}}(\text{L-threonine})(1,10\text{-phenanthroline})(\text{H}_2\text{O})](\text{ClO}_4)$

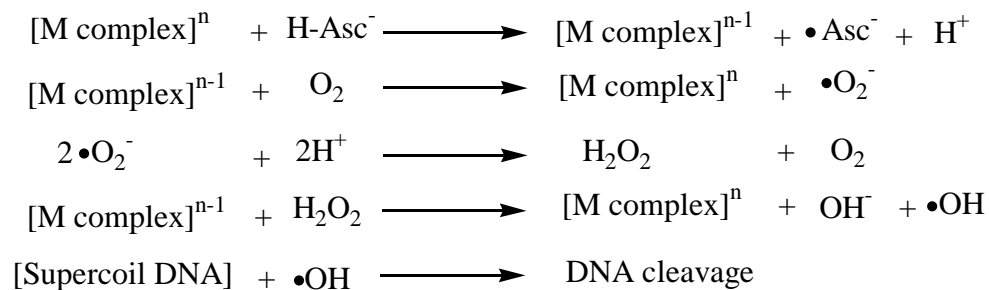


Figure 1.9: The proposed DNA cleavage mechanism of metal complex in the presence of ascorbic acid

1.3.3 Oxidative DNA cleavage by metal complexes in the presence of H₂O₂

Complexes [Co^{II}(imidazole-terpyridine)₂](ClO₄)₂ and [Cu^{II}(imidazole-terpyridine)₂](ClO₄)₂ (Figure 1.10) can promote oxidative DNA cleavage in the presence of H₂O₂ [37, 38]. In contrast to MPA and ascorbic acid, H₂O₂ acts as oxidation agent in the DNA cleavage reaction. Complex [Co^{II}(imidazole-terpyridine)₂](ClO₄)₂ can only induce single DNA scission by converting supercoil DNA to nicked form while complex [Cu^{II}(imidazole-terpyridine)₂](ClO₄)₂ can induce both single and double DNA scissions by converting supercoil DNA to nicked and linear forms. This indicates that the DNA cleavage efficiency of complex [Cu^{II}(imidazole-terpyridine)₂](ClO₄)₂ is higher than the DNA cleavage efficiency of complex [Co^{II}(imidazole-terpyridine)₂](ClO₄)₂ in the presence of H₂O₂. From the mechanistic studies, it is shown that the hydroxyl radical scavenger DMSO can reduce significantly the nuclease activity of complex [Co^{II}(imidazole-terpyridine)₂](ClO₄)₂ while the hydroxyl radical scavenger ethanol can reduce significantly the nuclease activity of complex [Cu^{II}(imidazole-terpyridine)₂](ClO₄)₂. This results reflect that the participation of hydroxyl radical in the cleavage process. The proposed DNA cleavage mechanism of metal complex in the presence of H₂O₂ is illustrated in Figure 1.11.

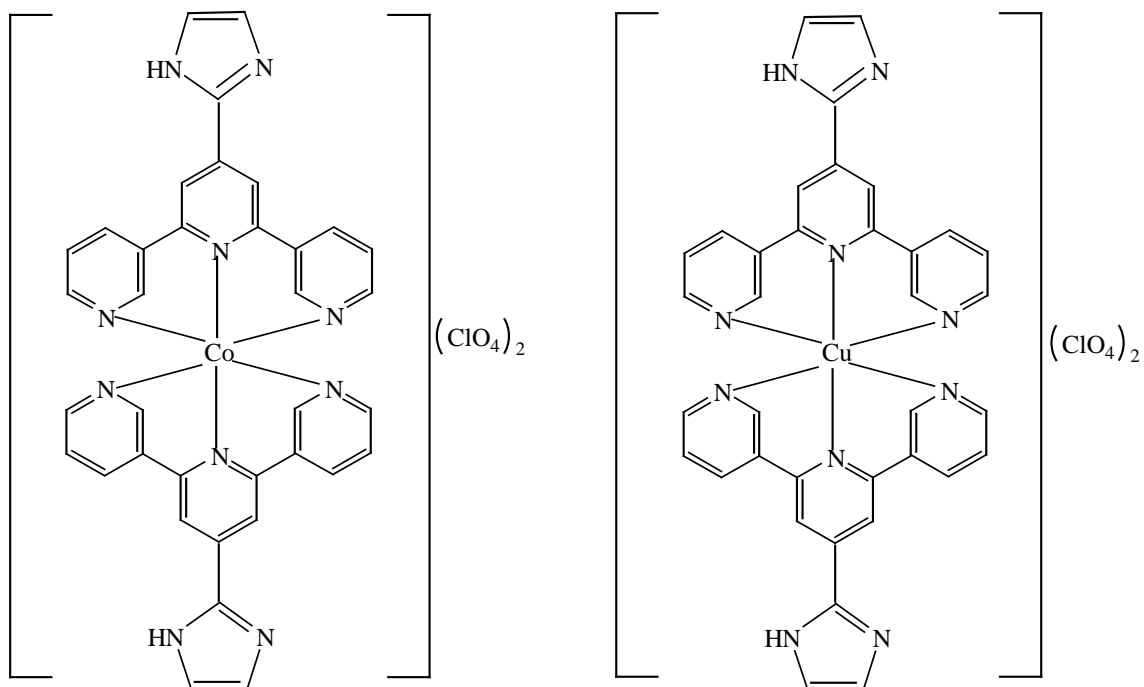


Figure 1.10: The schematic structures;
 a) $[\text{Co}^{\text{II}}(\text{imidazole-terpyridine})_2](\text{ClO}_4)_2$
 b) $[\text{Cu}^{\text{II}}(\text{imidazole terpyridine})_2](\text{ClO}_4)_2$

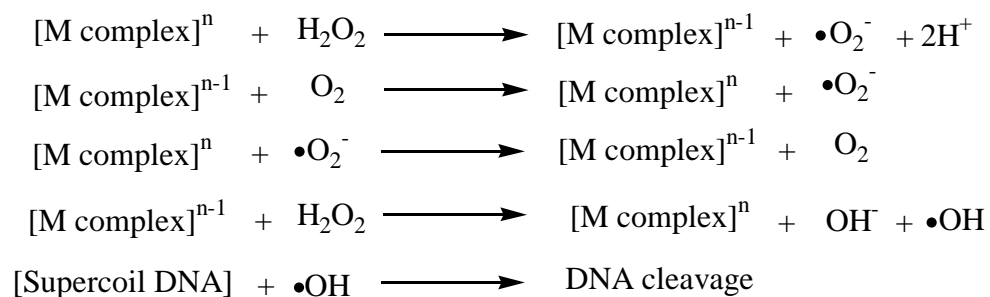


Figure 1.11: The proposed DNA cleavage mechanism of metal complex in the presence of H_2O_2

1.3.4 Photolytic DNA cleavage by metal complexes

Complexes $[\text{Cu}^{\text{II}}(\text{ternary-S-methyl-L-cysteine})(\text{dipyridoquinoxaline})(\text{H}_2\text{O})](\text{ClO}_4)$, $[\text{Co}^{\text{III}}(\text{ethylenediamine})_2(\text{imidazo}[4,5-f][1,10]\text{-phenanthroline})]\text{Br}_3$, $[\text{Ru}^{\text{II}}(2,2'\text{-bipyridine})_2(5\text{-methoxy-isatino-}[1,2-b]\text{-}1,4,8,9\text{-tetraazatriphenylene})](\text{ClO}_4)_2$ and $[\text{Ni}^{\text{II}}(\text{naphtho}[2,3-a]\text{dipyrido}[3,2-h:2',3'-f]\text{phenazine-}5,18\text{-dione})(1,10\text{-phenanthroline})](\text{PF}_6)_2$ (Figure 1.12) can trigger photolytic DNA cleavage upon irradiation [34, 39, 40, 41]. Complexes $[\text{Cu}^{\text{II}}(\text{ternary-S-methyl-L-cysteine})(\text{dipyridoquinoxaline})(\text{H}_2\text{O})](\text{ClO}_4)$ and $[\text{Ru}^{\text{II}}(2,2'\text{-bipyridine})_2(5\text{-methoxy-isatino-}[1,2-b]\text{-}1,4,8,9\text{-tetraaza triphenylene})](\text{ClO}_4)_2$ can induce both single and double DNA scissions by converting supercoil DNA to nicked and linear forms while complexes $[\text{Co}^{\text{III}}(\text{ethylenediamine})_2(\text{imidazo}[4,5-f][1,10]\text{-phenanthroline})]\text{Br}_3$ and $[\text{Ni}^{\text{II}}(\text{naphtho}[2,3-a]\text{dipyrido}[3,2-h:2',3'-f]\text{phenazine-}5,18\text{-dione})(1,10\text{-phenanthroline})](\text{PF}_6)_2$ can only induce single DNA scission by converting supercoil DNA to nicked form. In comparison, DNA cleavage efficiency of complexes $[\text{Ru}^{\text{II}}(2,2'\text{-bipyridine})_2(5\text{-methoxy-isatino-}[1,2-b]\text{-}1,4,8,9\text{-tetraazatriphenylene})](\text{ClO}_4)_2$ and $[\text{Cu}^{\text{II}}(\text{ternary-S-methyl-L-cysteine})(\text{dipyridoquinoxaline})(\text{H}_2\text{O})](\text{ClO}_4)$ is higher than the DNA cleavage efficiency of complexes $[\text{Co}^{\text{III}}(\text{ethylenediamine})_2(\text{imidazo}[4,5-f][1,10]\text{-phenanthroline})]\text{Br}_3$ and $[\text{Ni}^{\text{II}}(\text{naphtho}[2,3-a]\text{dipyrido}[3,2-h:2',3'-f]\text{phenazine-}5,18\text{-dione})(1,10\text{-phenanthroline})](\text{PF}_6)_2$ under photolytic DNA cleavage. In mechanistic studies, DNA cleavage activity of complexes $[\text{Ru}^{\text{II}}(2,2'\text{-bipyridine})_2(5\text{-methoxy-isatino-}[1,2-b]\text{-}1,4,8,9\text{-tetraazatriphenylene})](\text{ClO}_4)_2$ and $[\text{Cu}^{\text{II}}(\text{ternary-S-methyl-L-cysteine})(\text{dipyridoquinoxaline})(\text{H}_2\text{O})](\text{ClO}_4)$ can be inhibited by singlet oxygen inhibitor sodium azide which indicate the contribution of singlet oxygen in the cleavage process. The

DNA cleavage mechanism of the complexes $\text{Co}^{\text{III}}(\text{ethylenediamine})_2(\text{imidazo}[4,5\text{-}f][1,10]\text{-phenanthroline})\text{Br}_3$ and $[\text{Ni}^{\text{II}}(\text{naphtho}[2,3\text{-}a]\text{dipyrido}[3,2\text{-}h:2',3'\text{-}f]\text{phenazine-}5,18\text{-dione})(1,10\text{-phenanthroline})](\text{PF}_6)_2$ is still under investigation. It is proposed that photon from the excitation source excites the metal complexes, which then transfers the energy to the ground state oxygen molecule ($^3\text{O}_2$) and excites it to the $^1\Delta_g$ state ($^1\text{O}_2$). The proposed DNA cleavage mechanism of metal complex under irradiation is illustrated in Figure 1.13.

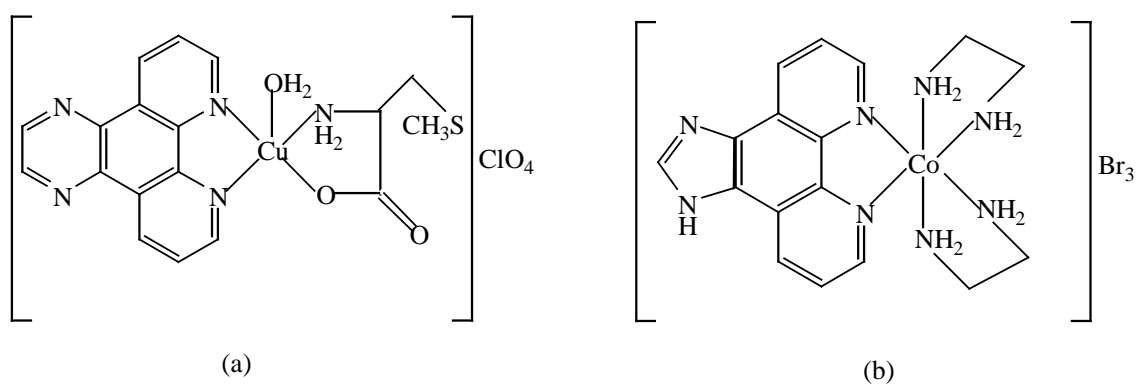
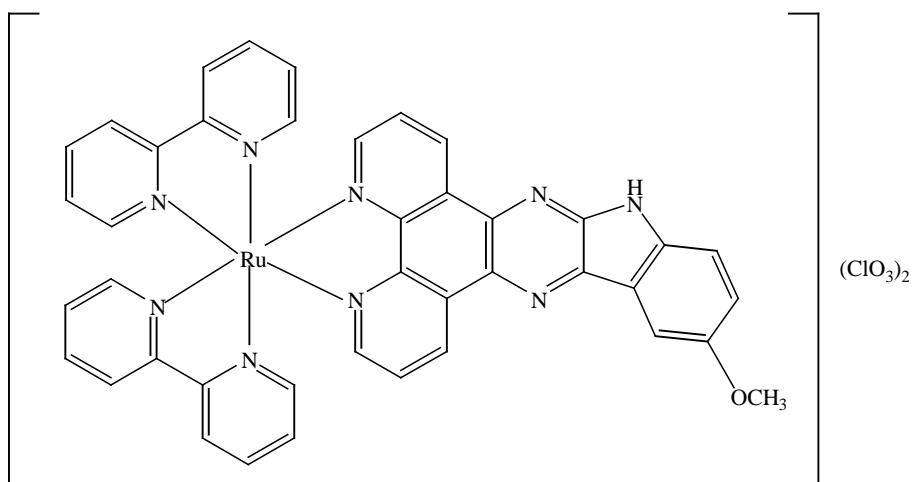
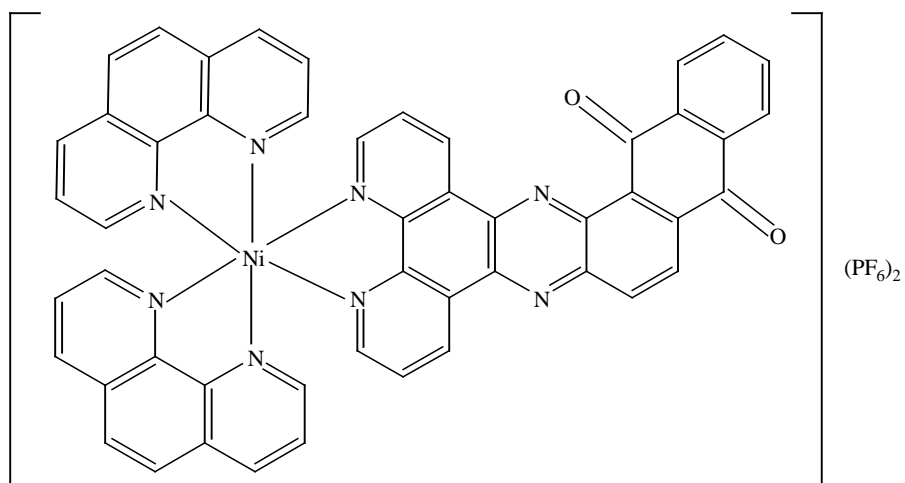


Figure 1.12: The schematic structures;

- a) $[\text{Cu}^{\text{II}}(\text{ternary-S-methyl-L-cysteine})(\text{dipyridoquinoxaline})(\text{H}_2\text{O})](\text{ClO}_4)$
- b) $[\text{Co}^{\text{III}}(\text{ethylenediamine})_2(\text{imidazo}[4,5\text{-}f][1,10]\text{-phenanthroline})]\text{Br}_3$



(c)



(d)

Figure 1.12: Continued

c) $[\text{Ru}^{\text{II}}(2,2'\text{-bipyridine})_2(5\text{-methoxy-isatino-[1,2-b]-1,4,8,9-tetraaza triphenylene)](\text{ClO}_4)_2$

d) $[\text{Ni}^{\text{II}}(\text{naphtho}[2,3\text{-}a]\text{dipyrido}[3,2\text{-}h:2',3'\text{-}f]\text{phenazine-5,18-dione})(1,10\text{-phenanthroline})](\text{PF}_6)_2$

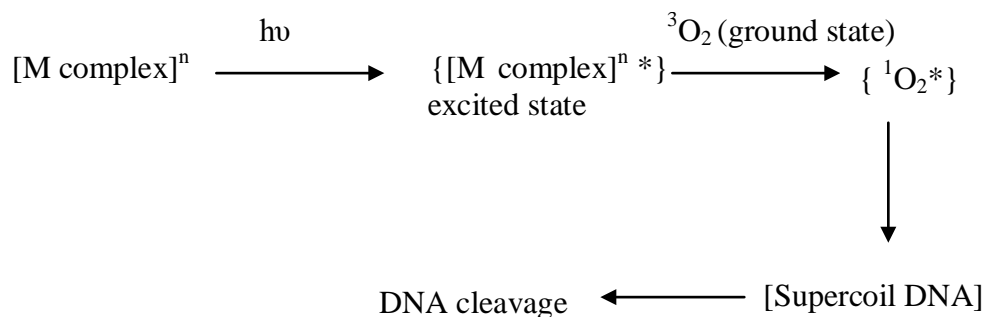
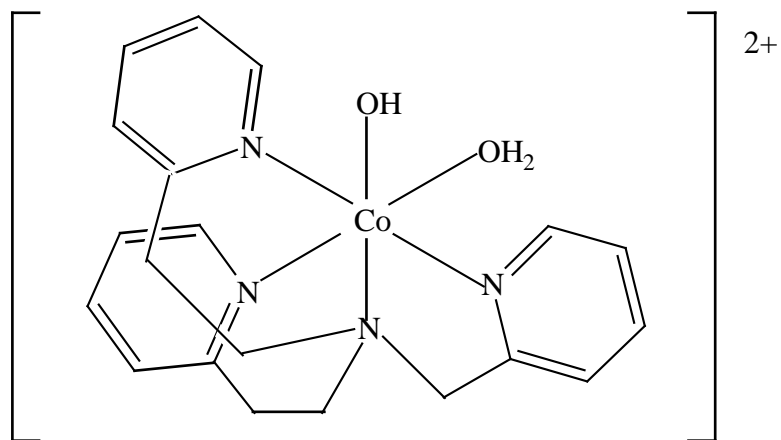


Figure 1.13: The proposed DNA cleavage mechanism of metal complex upon irradiation

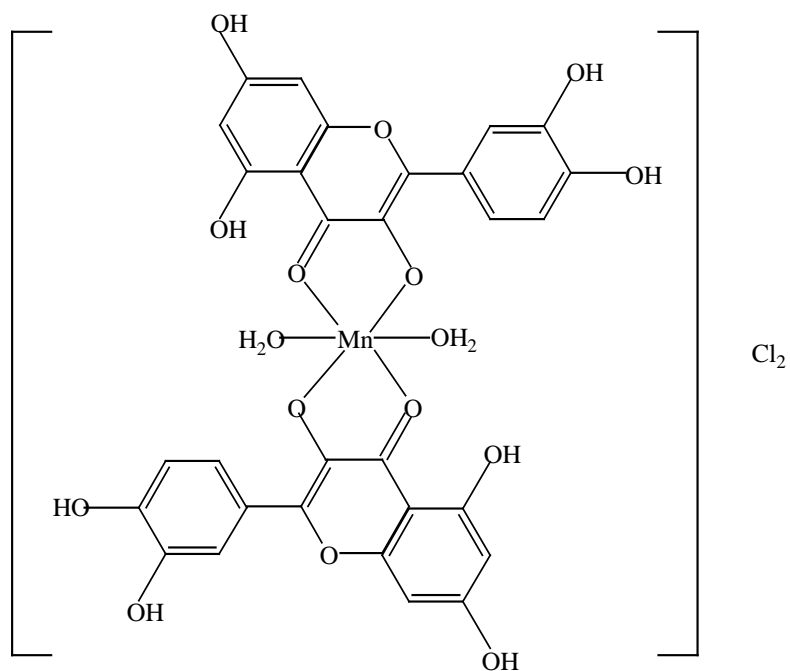
1.3.5 Hydrolytic DNA cleavage by metal complexes

Cis-aquahydroxo-tetraamine-cobalt(III) complex, $[\text{Co}^{\text{III}}(\text{bis}[2-(2\text{-pyridylethyl)}](2\text{-pyridylmethyl)amine})(\text{OH})(\text{H}_2\text{O})]^{2+}$, generated from $[\text{Co}^{\text{III}}(\text{bis}[2-(2\text{-pyridylethyl)}](2\text{-pyridylmethyl)amine})(\text{CO}_3)]\text{ClO}_4$ and complex $[\text{Mn}^{\text{II}}(\text{quercetin})_2(\text{H}_2\text{O})_2]\text{Cl}_2$ (Figure 1.14) can induce DNA cleavage via hydrolytic pathway [42, 43]. Both of the complexes can induce DNA cleavage in the absence of co-factor and in the dark. The mechanistic aspects of the DNA cleavage reaction have been investigated with various inhibiting agents and the results show that hydroxyl radical and singlet oxygen scavengers cannot inhibit the DNA cleavage induced by both of the complexes. These observations indicate that hydroxyl radical and singlet oxygen species are not involved in the cleavage reaction. The DNA cleavage characteristics of complexes $[\text{Co}^{\text{III}}(\text{bis}[2-(2\text{-pyridylethyl)}](2\text{-pyridylmethyl)amine})(\text{OH})(\text{H}_2\text{O})]^{2+}$ and $[\text{Mn}^{\text{II}}(\text{quercetin})_2(\text{H}_2\text{O})_2]\text{Cl}_2$ support hydrolytic cleavage. Both of the complexes can induce single and double DNA scissions by converting supercoil DNA to nicked and linear forms. In hydrolytic cleavage, it is

proposed that DNA cleavage occurs at the P–O bond in the phosphodiester of DNA. The proposed hydrolytic DNA cleavage mechanism by metal complex is illustrated in Figure 1.15.



(a)



(b)

Figure 1.14: The schematic structures;

- a) $[\text{Co}^{\text{III}}(\text{bis}[2-(2\text{-pyridylethyl})](2\text{-pyridylmethyl)amine})(\text{OH})(\text{H}_2\text{O})]^{2+}$
 b) $[\text{Mn}^{\text{II}}(\text{quercetin})_2(\text{H}_2\text{O})_2]\text{Cl}_2$

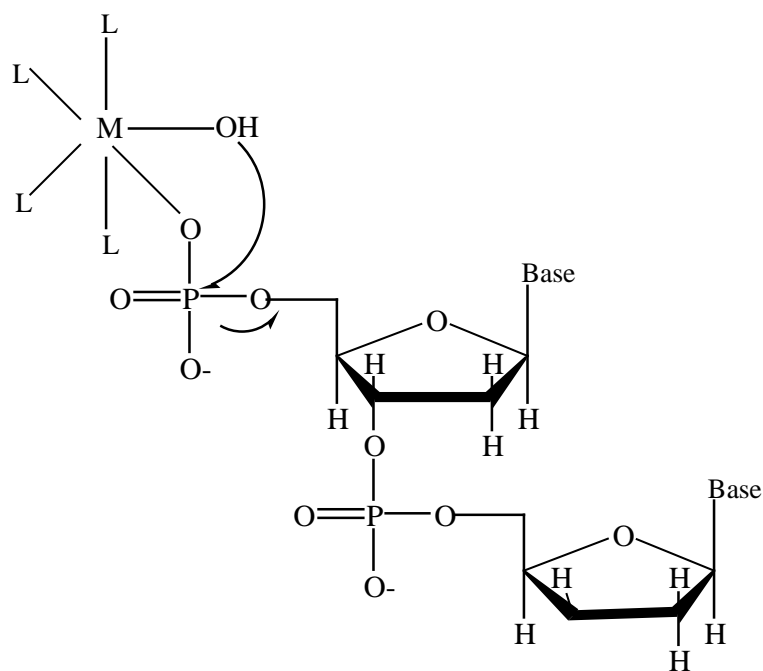


Figure 1.15: The proposed hydrolytic DNA cleavage mechanism by the metal complex

1.3.6 Oxidative DNA cleavage by copper(II) amino acid complexes in the presence of H_2O_2

Recently, Ng et al. have demonstrated that neutral Cu^{II} amino acid complexes such as $\text{Cu}^{\text{II}}(\text{N,N-di-}(N'\text{-methylacetamido})\text{-L-alaninato})_2$ and $\text{Cu}^{\text{II}}(\text{N,N'-dimethylglycinato})_2$ (Figure 1.16) can induce oxidative cleavage of DNA in the presence of H_2O_2 [44, 45]. Both of the complexes can induce single and double DNA scissions by converting supercoil DNA to nicked and linear forms. Hydroxyl radical scavenger DMSO can inhibit significantly the cleavage reaction induced by complex $\text{Cu}^{\text{II}}(\text{N,N}'\text{-$

dimethylglycinato)₂ which reflect the involvement of hydroxyl radical in cleavage reaction. The proposed DNA cleavage mechanism by complex Cu^{II}(N,N'-dimethylglycinato)₂ is similar to the proposed DNA cleavage mechanism illustrated in Figure 1.11.

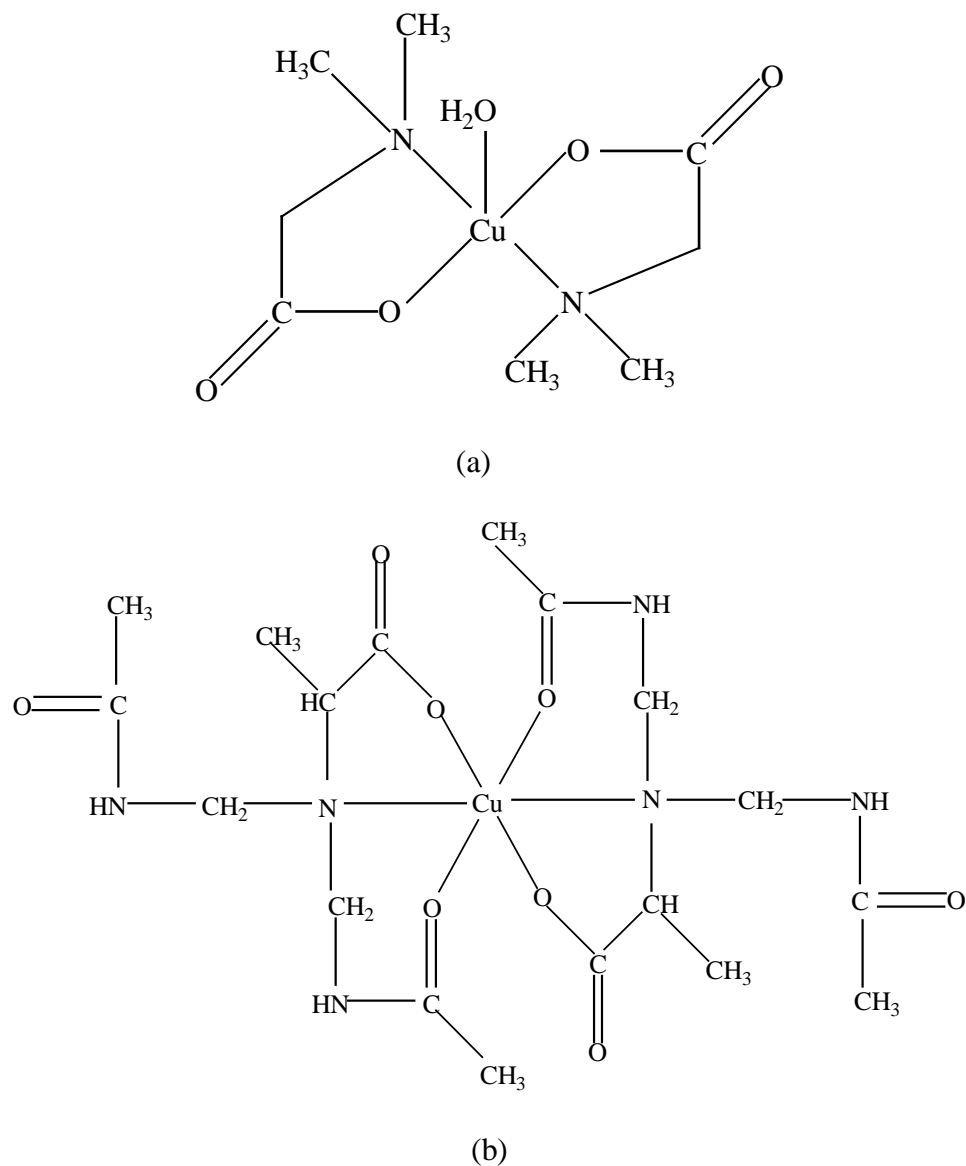


Figure 1.16: The schematic structures;
 a) Cu^{II}(N,N'-dimethylglycinato)₂
 b) Cu^{II}(N,N-di-(N'-methylacetamido)-L-alaninato)₂